

An excess of dusty starbursts related to the Spiderweb galaxy

H. Dannerbauer¹, J. D. Kurk², C. De Breuck³, D. Wylezalek³, J. S. Santos⁴, Y. Koyama^{5,6}, N. Seymour⁷, M. Tanaka^{5,8}, N. Hatch⁹, B. Altieri¹⁰, D. Coia¹⁰, A. Galametz¹¹, T. Kodama⁵, G. Miley¹², H. Röttgering¹², M. Sanchez-Portal¹⁰, I. Valtchanov¹⁰, B. Venemans¹³, and B. Ziegler¹

¹ Universität Wien, Institut für Astrophysik, Türkenschanzstraße 17, 1180 Wien, Austria
e-mail: helmut.dannerbauer@univie.ac.at

² Max-Planck-Institut für extraterrestrische Physik, Giessenbachstraße 1, 85748 Garching, Germany

³ European Southern Observatory, Karl Schwarzschild Straße 2, 85748, Garching, Germany

⁴ INAF-Osservatorio Astrofisico di Arcetri, Largo E. Fermi 5, 50125, Firenze, Italy

⁵ Optical and Infrared Astronomy Division, National Astronomical Observatory of Japan, Mitaka, Tokyo 181-8588, Japan

⁶ Institute of Space Astronomical Science, Japan Aerospace Exploration Agency, Sagami-hara, Kanagawa 252-5210, Japan

⁷ International Centre for Radio Astronomy Research, Curtin University, Perth, Australia

⁸ Kavli Institute for the Physics and Mathematics of the Universe, The University of Tokyo, 5-1-5 Kashiwanoha, Kashiwa-shi, Chiba 277-8583, Japan

⁹ School of Physics and Astronomy, University of Nottingham, University Park, Nottingham NG7 2RD, UK

¹⁰ Herschel Science Centre, European Space Astronomy Centre, ESA, 28691 Villanueva de la Cañada, Spain

¹¹ INAF - Osservatorio di Roma, via Frascati 33, 00040, Monteporzio, Italy

¹² Leiden Observatory, PO Box 9513, 2300 RA Leiden, the Netherlands

¹³ Max-Planck Institut für Astronomie, Königstuhl 17, 69117 Heidelberg, Germany

Received 7 March 2014; accepted XX 2014

ABSTRACT

We present APEX LABOCA 870 μm observations of the field around the high-redshift radio galaxy MRC1138–262 at $z = 2.16$. We detect 16 submillimeter galaxies in this $\sim 140 \text{ arcmin}^2$ bolometer map with flux densities in the range 3 – 11 mJy. The raw number counts indicate a density of submillimeter galaxies (SMGs) that is up to four times that of blank field surveys. Based on an exquisite multiwavelength database, including VLA 1.4 GHz radio and infrared observations, we investigate whether these sources are members of the protocluster structure at $z \approx 2.2$. Using *Herschel* PACS+SPIRE and *Spitzer* MIPS photometry, we derive reliable far-infrared photometric redshifts for all sources. Follow-up VLT ISAAC and SINFONI near-infrared spectra confirm that four of these SMGs have redshifts of $z \approx 2.2$. We also present evidence that another SMG in this field, detected earlier at 850 μm , has a counterpart that exhibits $\text{H}\alpha$ and CO(1-0) emission at $z=2.15$. Including the radio galaxy and two SMGs with far-IR photometric redshifts at $z=2.2$, we conclude that at least eight submm sources are part of the protocluster at $z = 2.16$ associated with the radio galaxy MRC1138–262. We measure a star formation rate density $\text{SFRD} \sim 1500 M_{\odot} \text{ yr}^{-1} \text{ Mpc}^{-3}$, four magnitudes higher than the global SFRD of blank fields at this redshift. Strikingly, these eight sources are concentrated within a region of 2 Mpc (the typical size of clusters in the local universe) and are distributed within the filaments traced by the $\text{H}\alpha$ emitters at $z \approx 2.2$. This concentration of massive, dusty starbursts is not centered on the submillimeter-bright radio galaxy which could support the infalling of these sources into the cluster center. Approximately half (6/11) of the SMGs that are covered by the $\text{H}\alpha$ imaging data are associated with $\text{H}\alpha$ emitters, demonstrating the potential of tracing SMG counterparts with this population. To summarize, our results demonstrate that submillimeter observations may enable us to study (proto)clusters of massive, dusty starbursts.

Key words. Galaxies: individual: MRC1138–262 — Galaxies: clusters: individual: MRC1138–262 — Galaxies: high redshift — Cosmology: observations — Infrared: galaxies — Submillimeter: galaxies

1. Introduction

The questions of when and how present-day galaxy clusters formed at high redshift have driven extensive searches for protoclusters of galaxies in the distant Universe in the past two decades (e.g., Le Fevre et al., 1996; Steidel et al., 1998; Pentericci et al., 2000; Kurk et al., 2000, 2004a,b; Best et al., 2003; Matsuda et al., 2005; Daddi et al., 2009a; Galametz et al., 2010, 2012; Hatch et al., 2011a,b; Mayo et al., 2012; Walter et al., 2012; Wylezalek et al., 2013). Powerful high-redshift radio galaxies (HzRGs; see the review by Miley & De Breuck, 2008) are considered to be the most promising signposts of the most massive clusters in formation. Surveys of Ly α emitters (LAEs), $\text{H}\alpha$ emitters (HAEs), Lyman break galaxies (LBGs), and extremely red objects (EROs) in

several fields containing radio galaxies, up to redshifts of 5.2, produced evidence of galaxy overdensities in almost all cases (e.g., Kurk et al., 2000; Miley et al., 2006; Overzier et al., 2006; Pentericci et al., 2000; Venemans et al., 2002, 2004, 2005, 2007), even out to 10 Mpc (Intema et al., 2006). These surveys convincingly demonstrate that HzRGs are good signposts of overdensities of galaxies at high redshift, at least in optical and near-infrared bands.

In the past decade (sub)millimeter surveys have revolutionized our understanding of the formation and evolution of galaxies by revealing a population of high-redshift, dust-obscured galaxies that are forming stars at a tremendous rate. Submillimeter galaxies (SMGs; see the review by Blain et al., 2002), first discovered by Smail et al. (1997), have intense star

formation, with rates of a few hundred to several thousand solar masses per year, but due to strong dust obscuration inconspicuous at optical/NIR wavelengths (e.g., Dannerbauer et al., 2002, 2004). These dusty starbursts are massive (a few times $10^{11} M_{\odot}$, see e.g., Genzel et al., 2003; Greve et al., 2005), and are probably the precursors of present-day ellipticals (e.g., Lutz et al., 2001; Ivison et al., 2013). Furthermore, SMGs are not uniformly distributed (Hickox et al., 2012) and are excellent tracers of mass density peaks (Ouchi et al., 2004) and thus of so-called protoclusters — the precursors of structures seen in the local universe such as the Coma cluster. These early (proto)clusters place significant constraints on models of galaxy assembly at those redshifts (Stern et al., 2010), and offer us a unique opportunity to explore episodes of bursting star formation in a critical epoch of galaxy formation.

Up to now, large scale structures like overdensities of galaxies have only been found through optical/near-infrared observations. However, we note that these optical and NIR techniques mainly trace (rather low-mass) galaxies with unobscured star formation, making up only 50% of the cosmic star formation activity (Dole et al., 2006). As outlined above, overdensities of unobscured star forming galaxies have been detected around a significant sample of HzRGs, but the detection of obscured star forming galaxies in these fields is lagging behind. Several studies report an excess of SMGs near HzRGs and QSOs (e.g., Stevens et al., 2003; De Breuck et al., 2004; Greve et al., 2007; Priddey et al., 2008; Stevens et al., 2010; Carrera et al., 2011; Rigby et al., 2014). However, the recent analysis of *Herschel* observations of the field of 4C+41.17 at $z = 3.8$ by Wylezalek et al. (2013) illustrates the importance of determining the redshifts of the SMGs. Wylezalek et al. (2013) show that most of the *Herschel* sources are foreground to the radio galaxy, casting doubts on the earlier claim from Ivison et al. (2000) of an overdensity related to the radio galaxy based on SCUBA observations.

One of the best studied large scale structures so far is the protocluster associated with the HzRG MRC1138–262 at $z = 2.16$, the so-called Spiderweb galaxy (Miley et al., 2006). Ly α and H α imaging/spectroscopy of this field reveal an excess of LAEs compared to blank fields (Kurk et al., 2000; Pentericci et al., 2000; Kurk et al., 2004a,b; Hatch et al., 2011b). Two attempts to search for submillimeter overdensities on this field are known. Using SCUBA, Stevens et al. (2003) report the (tentative) excess of SMGs, and spatial extension of the submillimeter emission of the HzRG MRC1138–262. However, we note that the field of view of SCUBA only has a diameter of $2'$ (~ 1 Mpc at $z = 2.16$), and thus the reported SMG excess is based on very small numbers. Rigby et al. (2014) present *Herschel* SPIRE observations of a larger field (~ 400 arcmin 2), centered on the HzRG. They report an excess of SPIRE $500 \mu\text{m}$ sources but found no filamentary structure in the far infrared as seen in the rest-frame optical (Kurk et al., 2004a; Koyama et al., 2013a). However, in both cases no counterpart identification was attempted for the individual sources. In addition, Valtchanov et al. (2013) report the serendipitous discovery of an overdensity of SPIRE $250 \mu\text{m}$ sources $7'$ south of the protocluster. Based on the modified black-body derived redshift distribution, incorporating both the color information and the SED shape, they conclude that the majority of the $250 \mu\text{m}$ sources in the overdensity are likely to be at a similar redshift. With the available scarce multiwavelength data they cannot exclude the attractive possibility that the overdensity is within the same structure as the Spiderweb at $z \approx 2.2$.

In this paper, we present our search for SMGs in the field of MRC1138–262 using APEX LABOCA $870 \mu\text{m}$ observations.

We discover 16 LABOCA sources, which is a significant excess of SMGs compared to blank field surveys. We identify the counterparts of the SMGs using the existing exquisite multi-wavelength data on this field (Pentericci et al., 2000; Kurk et al., 2004a,b; Seymour et al., 2012; Koyama et al., 2013a). The main aim of this work is to verify how many of the 16 SMGs are part of the well-known protocluster structure at $z \approx 2.2$. We mainly focus on *Spitzer* MIPS, *Herschel* PACS+SPIRE, and VLA data, complemented by narrow-band images of H α emitters (HAEs) at $z \approx 2.2$. We show that H α emitters can readily be used to identify the counterparts of SMGs since several SMGs are bright in H α .

The structure of this paper is as follows. Sections 2 and 3 describe the observations of the field around the HzRG MRC1138–262 and the associated LABOCA sources. In Section 4 we present the method for deriving far-infrared photometric redshifts, luminosities and star formation rates for the LABOCA sources. In Section 5 we discuss the sources individually and in Section 6 the properties of the SMG overdensity. We adopt the cosmological parameters $\Omega_{\text{matter}} = 0.27$, $\Omega_{\Lambda} = 0.73$, and $H_0 = 71 \text{ km s}^{-1} \text{ Mpc}^{-1}$ (Spergel et al., 2003, 2007).

2. Observations and data reduction

2.1. LABOCA imaging

We mapped a field of ~ 140 arcmin 2 around the HzRG MRC1138–262 with the bolometer camera LABOCA (Siringo et al., 2009) installed on the APEX telescope through ESO (ID: 084.A-1016(A), PI: J. D. Kurk) and Max-Planck-Gesellschaft (MPG, ID: 083.F-0022, PI: J. D. Kurk) time. The LABOCA instrument contains 295 bolometer elements and operates at an effective frequency of 345 GHz corresponding to $870 \mu\text{m}$. The LABOCA array covers a field of view of $11.4'$ with a FWHM of $19''$ at $870 \mu\text{m}$. The observations were taken between August and December 2009 in service mode, under

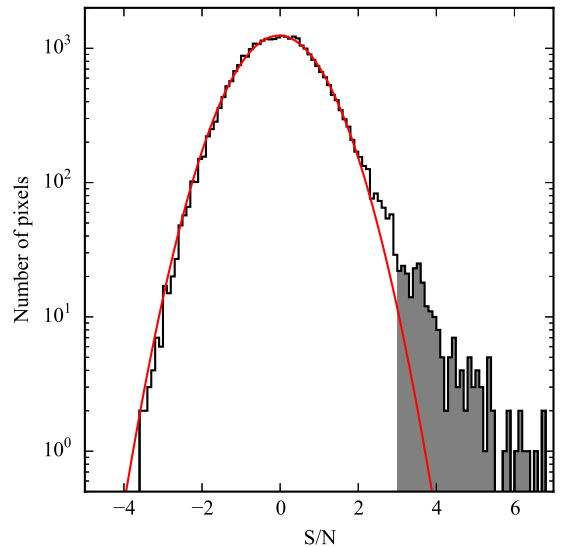


Fig. 1. Histogram of the pixel signal-to-noise values of our LABOCA map. The red solid line shows a gaussian fit. The significant excess of pixels with a $S/N \geq 3\sigma$ is shown in grey. Almost all of these pixels belong to selected sources and none to pixels at the edge of the map.

excellent atmospheric conditions with typical zenith opacities between 0.2 and 0.3 at 870 μm . The total on sky integration time was 16.6 hours.

We used the raster spiral scanning mode which combines the spiral scanning pattern with raster mapping. This mode has the advantage of producing a fully sampled map of the total field-of-view of LABOCA in a dense sampling pattern. The calibration observations were performed on a regular basis and included pointing, focus and flux calibration, see Siringo et al. (2009) for more details. Each scan was carefully inspected for the presence of possible outliers, anomalies, and the influence of instabilities in the atmosphere. The data were reduced using *miniCrush* (Kovács, 2008), a commonly used software for the reduction of (sub)millimeter bolometric data. We used the option ‘*deep*’ that is optimized for the reduction of deep field data containing faint, point-like sources. The end product of the *miniCrush* reduction is a multi-frame FITS image containing a signal map, a noise map, a signal-to-noise map and an exposure time map.

In the central part of the LABOCA map ($\sim 56 \text{ arcmin}^2$), we achieve an rms noise level of 1.3–1.9 mJy. In Fig. 1, we show the pixel signal-to-noise distribution of our LABOCA map. The main distribution of pixel values are well fit by a Gaussian centered at zero. However, there is significant excess of positive valued pixels with a signal-to-noise ratio (S/N) $\geq 3\sigma$. This skewed distribution indicates that the pixels with excess are associated with real submillimeter sources. We have checked this by identifying all pixels with a $S/N \geq 3\sigma$ on the map and confirmed that almost all of these belong to sources identified in Section 5 and none lie near the edge of the map.

We have searched our LABOCA signal-to-noise map within the region where the noise is $\sigma < 3.0 \text{ mJy/beam}$ (Fig. 2) for S/N peaks down to 3.5σ . Furthermore, we cross-identified LABOCA S/N peaks below 3.5σ which are detected at similar submm wavelengths, in our case by *Herschel* (see below this and subsection 2.3 for more details) as potential LABOCA sources. The detected sources had to have at least the size of the LABOCA beam. In Table 1 we list all 16 sources in order of signal-to-noise and from now on we use their alias (DKB01–DKB16). Twelve LABOCA sources are classified as secure ($S/N \geq 3.5$), the remaining four sources are classified as cross-identified tentative. We give the position of the pixel with the highest S/N and list the peak fluxes — a standard technique in radio astronomy — obtained from the signal map. We used two approaches to verify the reliability of our selected sources. The first approach relies on checking observations of the same field at similar wavelengths. We use our *Herschel* PACS+SPIRE dataset, see forthcoming section 2.3 for more details. With these deep and wide ‘auxiliary’ *Herschel* data, we can very well discard spurious LABOCA sources. Only one out of 16 sources (DKB09) is not detected at any of the *Herschel* bands. Especially, all of the four ‘tentative’ LABOCA sources have significantly detected *Herschel* counterparts, see also Table 2. The second approach is based on the so-called jackknife technique: We split the ESO and MPG data into two groups of similar integration time. All 16 sources were detected in both datasets. Finally, we investigated the reliability of our source extraction approach. For this sanity check, we used the source extraction tool *detect*, part of the software package *Crush* (Kovács, 2008). Beside the 2.4σ source, all sources could be recovered by this extraction algorithm down to 3.0σ , giving us faith in our approach. For sources with $\geq 3.5\sigma$, the false detection rate is estimated on 0.2 sources among the 12 secure sources, justifying that we call this sample secure. To guarantee a proper comparison with the only known

LABOCA deep field on the ECDFS (LESS Weiß et al., 2009), we used only our 3.7σ sources for surface density calculations.

2.2. VLA imaging

The MRC 1138-262 field was observed with the Karl G. Jansky Very Large Array (VLA; Napier, Thompson & Ekers, 1983) on UT 2002 April 1-12 for a total of 12 hours in A configuration at 20 cm (ID: AD0463, PI: C. De Breuck). We observed in a pseudo-continuum, spectral line mode with $7 \times 3.125 \text{ MHz}$ channels. The point source 1351–148 was monitored every 40 min to obtain amplitude, phase and bandpass calibration, and an observation of 3C 286 was used to obtain the absolute flux calibration.

Standard spectral-line calibration and editing of the data was performed using the NRAO *ATPS* package and standard wide field imaging techniques (Taylor, Carilli, & Perley, 1999). The final 7.5×7.5 image has an rms noise level of $19 \mu\text{Jy beam}^{-1}$, except in an area close to the central radio galaxy which is limited by the ability to clean the bright radio source. The dynamic range achieved is $\sim 10^4$. The FWHM resolution of the restoring beam is $2''.7 \times 1''.3$ at a position angle $\text{PA} = -10^\circ$.

2.3. Panchromatic observations

To analyse the 16 LABOCA sources we used several additional data sets (see also Fig. 9):

- *H α spectroscopy*: In February 2012 we conducted VLT ISAAC long-slit near-infrared spectroscopic observations (ID: 088.A-0754(A), PI: J. D. Kurk) of the redshifted *H α* line in visitor mode in order to confirm the redshifts of several LABOCA sources that were likely to be protocluster members. A detailed discussion of these observations will be presented in Kurk et al. (in prep.). In the current paper we only use the redshifts from these NIR spectra for our analysis and discussion. Furthermore, very recently we obtained VLT SINFONI IFU spectroscopy (ID: 090.B-0712(A), PI: J. D. Kurk) data of four likely merging galaxies at $z \approx 2.2$ that are in the LABOCA FWHM of one of the SMGs.
- *H α imaging*: A total area of $\sim 50 \text{ arcmin}^2$ was imaged with the MOIRCS camera on the SUBARU telescope using a narrow-band filter covering *H α* emitted at the redshift of the radio galaxy (for a detailed description see Koyama et al., 2013a). The narrow-band filter NB2071 ($\lambda = 2.068 \mu\text{m}$, $\Delta\lambda = 0.027 \mu\text{m}$) covered the redshift range $z = 2.13 - 2.17$. These data encompassed the smaller ($\sim 12 \text{ arcmin}^2$) but deeper *H α* data taken with the VLT ISAAC by Kurk et al. (2004a,b).
- *Ly α imaging*: A subsection of the LABOCA field ($\sim 49 \text{ arcmin}^2$) was imaged in *Ly α* redshifted to $z = 2.16$. Details of these observations can be found in Kurk et al. (2000, 2004a).
- *Herschel data*: This field was observed in the far-IR with the instruments PACS and SPIRE onboard of the *Herschel* Space Observatory (Pilbratt et al., 2010; Poglitsch et al., 2010; Griffin et al., 2010) as part of the project scientist guaranteed time (PI: B. Altieri). These observations are presented in detail in Seymour et al. (2012) and Valtchanov et al. (2013). The PACS images achieve 3σ sensitivities of $\sim 4.5 \text{ mJy}$ and $\sim 9.0 \text{ mJy}$ at $100 \mu\text{m}$ and $160 \mu\text{m}$, respectively. The SPIRE images achieve 3σ sensitivities of $\sim 7.5 \text{ mJy}$, $\sim 8.0 \text{ mJy}$ and $\sim 9.0 \text{ mJy}$ at $250 \mu\text{m}$, $350 \mu\text{m}$ and $500 \mu\text{m}$, respectively. The size of the PACS and SPIRE maps are $\sim 120 \text{ arcmin}^2$ and $\sim 900 \text{ arcmin}^2$ respectively (Valtchanov et al., 2013). The entire LABOCA map is covered by the SPIRE data and almost completely covered by PACS.

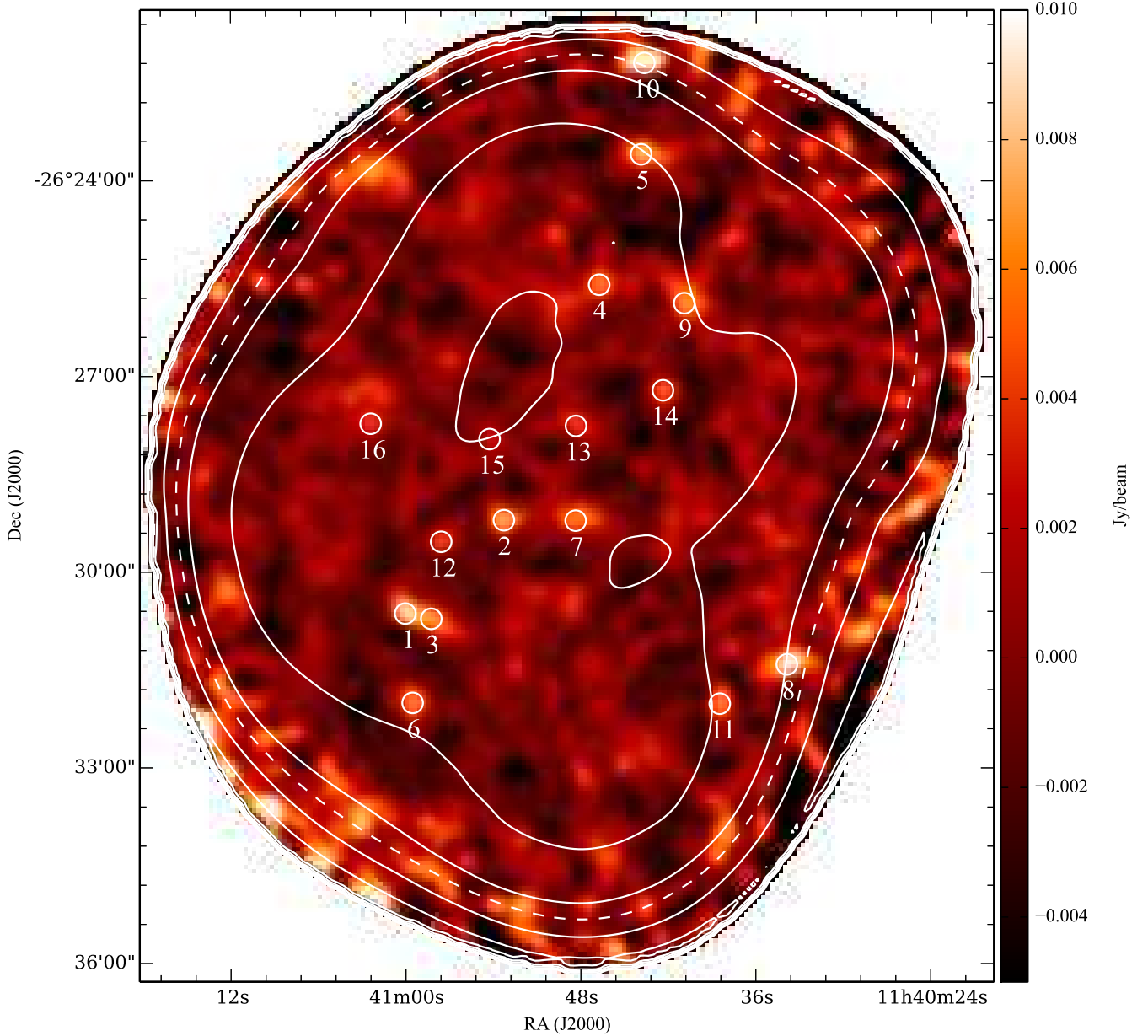


Fig. 2. LABOCA signal map of the field around the high- z radio galaxy MRC1138–262 (# 7). Encircled, we show the location of 16 SMGs extracted from our LABOCA map. Contours indicate the noise at 1.3, 1.9, 2.6, 3.0, 3.7, 5.2 and 7.4 mJy/beam. The dashed contour encompasses the region where the noise is $\sigma < 3.0$ mJy/beam, including all selected 16 LABOCA sources. The source density is up to $4\times$ higher than in the ECDFS. North is at the top and east is to the left.

There is also a wider SPIRE map (~ 30 arcmin radius) of similar depth that is presented in Rigby et al. (2014), however the extended regions are not required for the present analysis.

- *Spitzer MIPS 24 μ m imaging:* We use archival *Spitzer* $5' \times 5'$ MIPS 24 μ m images which are centered on the HzRG and cover about 20% of the LABOCA image. These data are used to derive far-IR photometric redshifts and establish the SEDs of the LABOCA counterparts.

- *Optical/near-infrared photometric redshifts:* Tanaka et al. (2010) derived photometric redshifts based on *UGRIZJHK_s* and three IRAC channel photometry of the field covered by *Spitzer*.

3. LABOCA source counterparts

We searched for LABOCA counterparts within $9''.5$ of the LABOCA detection in the MIPS 24 μ m, PACS 100/160 μ m and VLA 1.4 GHz images (see Table 2). These wavelengths (in particular 1.4 GHz) are well suited for finding SMG counterparts and obtaining more precise positions than measured by the bolometer data (e.g., Dannerbauer et al., 2004, 2010; Pope et al., 2006). The search circle is consistent with the FWHM of the LABOCA beam and guarantees that no reliable associations are missed. For each candidate counterpart within the search radius we calculate the corrected Poissonian probability p that the SMG association is a chance coincidence. This approach corrects the simple Poissonian probability of a detected association for the possibility of associations of different nature but similar proba-

Table 1. 870 μm LABOCA Source Catalog of the Field of MRC1138–262

Source (IAU) (1)	Alias (2)	R.A. (J2000.0) (3)	Decl. (J2000.0) (4)	$S_{870\mu\text{m}}$ (mJy) (5)	S/N (6)
SMM 114100.0–263039	DKB01	11:41:00.04	–26:30:39.2	9.8 ± 1.5	6.7
SMM 114053.3–262913	DKB02	11:40:53.28	–26:29:14.0	8.1 ± 1.5	5.4
SMM 114058.3–263044	DKB03	11:40:58.26	–26:30:44.0	7.3 ± 1.5	4.9
SMM 114046.8–262539	DKB04	11:40:46.75	–26:25:39.2	6.8 ± 1.4	4.7
SMM 114043.9–262340	DKB05	11:40:43.88	–26:23:40.2	8.2 ± 1.8	4.5
SMM 114059.5–263200	DKB06	11:40:59.54	–26:32:00.7	6.8 ± 1.7	3.9
SMM 114048.4–262914	DKB07	11:40:48.36	–26:29:14.4	6.7 ± 1.7	3.9
SMM 114033.9–263125	DKB08	11:40:33.88	–26:31:25.6	10.6 ± 2.7	3.9
SMM 114040.9–262555	DKB09	11:40:40.92	–26:25:56.0	7.1 ± 1.9	3.8
SMM 114043.7–262216	DKB10	11:40:43.66	–26:22:16.8	11.0 ± 3.0	3.7
SMM 114038.5–263201	DKB11	11:40:38.48	–26:32:01.4	7.0 ± 1.9	3.6
SMM 114057.6–262933	DKB12	11:40:57.58	–26:29:33.7	5.0 ± 1.4	3.6
cross-identified tentative detections					
SMM 114048.3–262748	DKB13	11:40:48.34	–26:27:48.0	4.4 ± 1.5	3.0
SMM 114042.4–262715	DKB14	11:40:42.38	–26:27:15.5	5.3 ± 1.8	3.0
SMM 114054.3–262800	DKB15	11:40:54.26	–26:28:00.0	3.2 ± 1.3	2.4
SMM 114102.7–262746	DKB16	11:41:02.41	–26:27:46.0	4.2 ± 1.4	2.9

Notes. — Col. (1): LABOCA source. Col. (2): Short name of LABOCA source. Col. (3): J2000.0 right ascension of LABOCA source. Units of right ascension are hours, minutes, and seconds. Col. (4): J2000.0 declination of LABOCA source. Units of declination are degrees, arcminutes, and arcseconds. Col. (5): LABOCA flux. Col. (6): Signal-to-Noise of LABOCA detection.

bility (Downes et al., 1986) and is widely applied and accepted in the community (e.g., Ivison et al., 2002; Dannerbauer et al., 2004, 2010; Biggs et al., 2011; Smail et al., 2014). It basically depends on the search radius, the distance of the potential counterpart to the LABOCA source and the source surface density down to the flux level of the potential LABOCA counterpart. More recent work that uses this method for SMGs can be found e.g. in Biggs et al. (2011).

Several previous attempts to locate secure counterparts of SMGs have been done using optical and near-infrared broad-band images (e.g., Webb et al., 2003b), the most successful one is to use *Spitzer* IRAC data (e.g., Pope et al., 2006; Hainline et al., 2009; Biggs et al., 2011). However, finding counterparts by applying p-statistics on optical and near-infrared images has not been very successful (e.g., Webb et al., 2003b). This is primarily because of the high surface density of (faint) optical and near-infrared sources which are not associated to the far-IR and radio sources. Applying the p-statistic method is most promising using data with low surface densities of sources, such as radio or far-IR images. In addition to this we find counterparts to several LABOCA sources in the $H\alpha$ imaging data. This motivates us to test a new approach by applying the p-statistic method to the $H\alpha$ emitters in the field of MRC1138–262 (Koyama et al., 2013a); cf. with Smail et al. (2014) who associated [OII] emitters successfully in the field and at the redshift of the cluster Cl0218.3–0510 with SMGs selected in this region.

Due to the large beam size of the SPIRE data (FWHM = $18'' - 36''$) there is a large uncertainty in the measured position and source blending is a big problem. We therefore do not apply the p-statistic method to the SPIRE data. The derived probabilities of PACS, MIPS and $H\alpha$ emitter (HAE) associations are based on raw number counts in the LABOCA field. At all wavelengths we search for counterparts of SMGs down to a signal-to-noise of 3σ . Bright radio emission from MRC1138 causes spurious sources in the VLA map that can not be “cleaned”. We therefore decide to assess the reliability of VLA counterparts using published number counts from e.g. Fomalont et al.

(2006). Similar to e.g. Dannerbauer et al. (2010), we define the following quality criteria for assessing the robustness of identified candidate counterparts: we classify SMG associations with $p \leq 0.05$ as secure, and those with $0.05 < p \leq 0.10$ as possible or tentative counterparts. Below we briefly discuss the results of the associations at different wavelengths.

3.1. VLA 1.4. GHz counterparts

Due to the limited dynamic range caused by the strong emission of the radio galaxy itself, the VLA map is shallow in comparison to other deep VLA integrations of submillimeter fields (e.g., Morrison et al., 2010). Eight out of 16 LABOCA sources, including the radio galaxy, have a VLA counterpart down to 3σ . The shallow depth of the VLA map may explain the rather low identification rate of 50%, however it is consistent with previous identification rates which range between 40 to 60% (e.g., Ivison et al., 2002; Dannerbauer et al., 2004). There are no cases of multiple VLA counterparts to a single LABOCA source in the field of MRC1138–262 and all VLA associations are classified as secure counterparts with fluxes between 60 and 620 μJy . However, we note that mm-interferometric observations have recently shown that not all VLA sources within the (sub)mm bolometer beam produce (sub)mm emission (e.g., Younger et al., 2007; Barger et al., 2012; Karim et al., 2013; Hodge et al., 2013), so we must be cautious in the interpretation of the eight VLA counterparts.

3.2. PACS 100 and 160 μm counterparts

We uncover PACS counterparts for nine SMGs, corresponding to a PACS identification rate of 56% of our whole SMG sample (see Table 2 for details). We detect 9 (6) SMGs at 160 (100) μm . All PACS 100 μm LABOCA associations are also detected at 160 μm . Although the PACS data are shallower than that of the PEP data of GOODS-N (Lutz et al., 2011), we find a higher identification rate than that reported by Dannerbauer et al.

(2010) for the GOODS-N field. This could indicate that a significant fraction of LABOCA sources are at redshift $z = 2.16$, a redshift still accessible by *Herschel* PACS (see e.g. Fig. 3 in Dannerbauer et al., 2010). The $160\ \mu\text{m}$ measurements lie close to the far-IR peak so it is unsurprising that the number of PACS counterparts at $160\ \mu\text{m}$ is higher than at $100\ \mu\text{m}$ (see also Dannerbauer et al., 2010). We note that based on the corrected Poissonian probability p , each PACS detection within the bolometer beam (our search circle) is classified as an associated SMG counterpart, being consistent with the results reported by Dannerbauer et al. (2010). PACS fluxes of these dust-obscured sources range between 5.2 mJy to 530.9 mJy at $100\ \mu\text{m}$ and 15.7 mJy to 652.0 mJy at $160\ \mu\text{m}$. Due to the shallowness of the VLA data, two PACS counterparts are not detected in the radio regime.

3.3. MIPS $24\ \mu\text{m}$ counterparts

Due to the high surface density of MIPS $24\ \mu\text{m}$ sources compared to VLA or *Herschel* sources the p-statistic is not as useful as in the radio or far-infrared regime. However, for completeness we performed the p-statistic for MIPS sources as well. In total, seven LABOCA sources are covered by the *Spitzer* MIPS $24\ \mu\text{m}$ map. Except in one case (DKB13), VLA/HAE counterparts are associated with MIPS $24\ \mu\text{m}$ sources. However, only three of them are classified as secure. In two cases the MIPS $24\ \mu\text{m}$ detections would not have been classified as statistical possible associations demonstrating the very limited use of p-statistic applied on this source population.

3.4. $H\alpha$ emitting counterparts

Eleven LABOCA sources are covered by the map of $H\alpha$ emitters at $z = 2.16$, of which seven SMGs (DKB01, DKB03, DKB07, DKB08, DKB12, DKB16, DKB15) have $H\alpha$ emitters within their LABOCA beams. In three cases, DKB01, DKB07 and DKB12, we find two, three and four HAEs within the search radius, respectively. Thirteen HAEs from Koyama et al. (2013a) are LABOCA counterparts of which 10 are classified as robust counterparts and only three are tentative. Therefore, this seems to be a very promising approach in order to find SMG counterparts (with subarcsecond position accuracy) for a (proto)cluster with known redshift.

13 out of 83 $H\alpha$ emitters in the field of MRC1138 are correlated with SMGs. Koyama et al. (2013a) report 15 MIPS $24\ \mu\text{m}$ associations (classified as dusty $H\alpha$ emitters) out of 60 HAEs in the MIPS FOV of $5'\times 5'$. Interestingly, five out of 13 HAEs (covered by MIPS) have MIPS $24\ \mu\text{m}$ counterparts. The higher rate of MIPS associations is consistent with SMGs being dusty. Except for the HzRG, only two SMG counterparts identified as a HAE coincides with a robust VLA counterpart. Recent rest-frame $H\alpha$ spectroscopy (Kurk et al., in prep.) confirms the redshifts of seven HAEs which are associated with LABOCA sources.

The *Herschel* PACS detections at 100 and/or $160\ \mu\text{m}$ of all secure HAEs associated with LABOCA sources except one, reinforces our hypothesis that these sources are the true SMG counterparts. In the case of DKB12 all four HAEs are within/at the edge of the PACS $160\ \mu\text{m}$ detection (no detection at $100\ \mu\text{m}$). None of the remaining HAEs classified as tentative SMG counterparts and without redshift confirmation are detected by PACS. We primarily use the $H\alpha$ imaging data from Koyama et al.

(2013a) for our analysis, however, to be complete we check if there are more HAEs in the deeper data of Kurk et al. (2004a).

4. Far-infrared photometric redshifts, luminosities and star formation rates

We derive far-infrared photometric redshifts of the LABOCA sources to test the hypothesis of how many of the 16 LABOCA sources are part of the protocluster structure at $z = 2.2$. Since the launch of *Herschel* far-IR photometric redshift determination has been established as a reliable diagnostic tool in order to investigate SMGs (e.g., Amblard et al., 2010; Roseboom et al., 2012; Pearson et al., 2013; Swinbank et al., 2014). Our far-infrared photometric redshifts are calculated using the code *hyperz* (Bolzonella et al., 2000) which minimizes the reduced χ^2 to find the best photometric redshift solution.

We use both synthetic and empirical AGN and starburst templates from the SWIRE template library (Polletta et al., 2007) complemented with self-constructed SED templates. The latter are obtained by spline interpolation of the mid- and far-infrared emission from LABOCA sources with confirmed spectroscopic redshifts. The far-IR emission of submillimeter sources, particularly those at high redshift, will be a superposition of the emission from stellar-heated dust and AGN activity. In most cases SED template libraries are derived from low-redshift sources and therefore often fail in fitting the far-IR dust-bump for high redshift sources, whose shape can vary greatly due to differing contributions from starburst and AGN (e.g., Lagache et al., 2005; Polletta et al., 2007; Skibba et al., 2011).

We choose sources DKB07, 12c, 13, and 14, which cover a wide range of far-IR SED shapes, to derive empirical dust templates. The final set of templates consists of four empirical templates and ten templates from the SWIRE library covering a range of galaxy types (e.g., elliptical galaxies, spiral galaxies, QSOs), see also Table 3. The resulting χ^2 distribution and the best χ^2 are derived by considering all redshifts and all templates in the final set. Note that the final χ^2 curve shows the minimum χ^2 for the template set as a function of redshift and therefore is dependent on the template set used.

Due to the varying spatial coverage of the supplementary multiwavelength data there are some sources that lie out of the field in some photometric bands. These photometric data points are not included. In case of non-detections at certain wavelengths 3σ upper limits are taken into account by *hyperz*. The best fitting SED and χ^2 are shown in Fig. 3 and Fig. 4. 11 SMGs (without known redshifts) have best fit SEDs that are empirical demonstrating the big advantage of using empirical templates.

We test our photometric redshift analysis by only considering the far-IR emission, i.e. SPIRE and LABOCA photometry. We derive templates from the same sources as above but without the MIPS detection and use the same ten templates from the SWIRE library as before and fit to find the best redshift solution. The photometric redshifts found mostly agree with the previously determined redshifts. For one source (DKB15) the MIPS detection, however, is crucial and we fail to find the same redshift. Our exercise shows that if the far-IR peak and its Rayleigh-Jeans tail are well sampled by observations, we can construct reliable photometric redshifts from these data alone with typical uncertainties of 30% that allow us to conclude if a source can belong to a structure associated with MRC1138 or not. If this is not the case then shorter wavelength data are crucial for constraining photometric redshifts. We note that redshifted [CII] emission contributes to the SPIRE $500\ \mu\text{m}$ flux for sources at $z \approx 2.2$, see

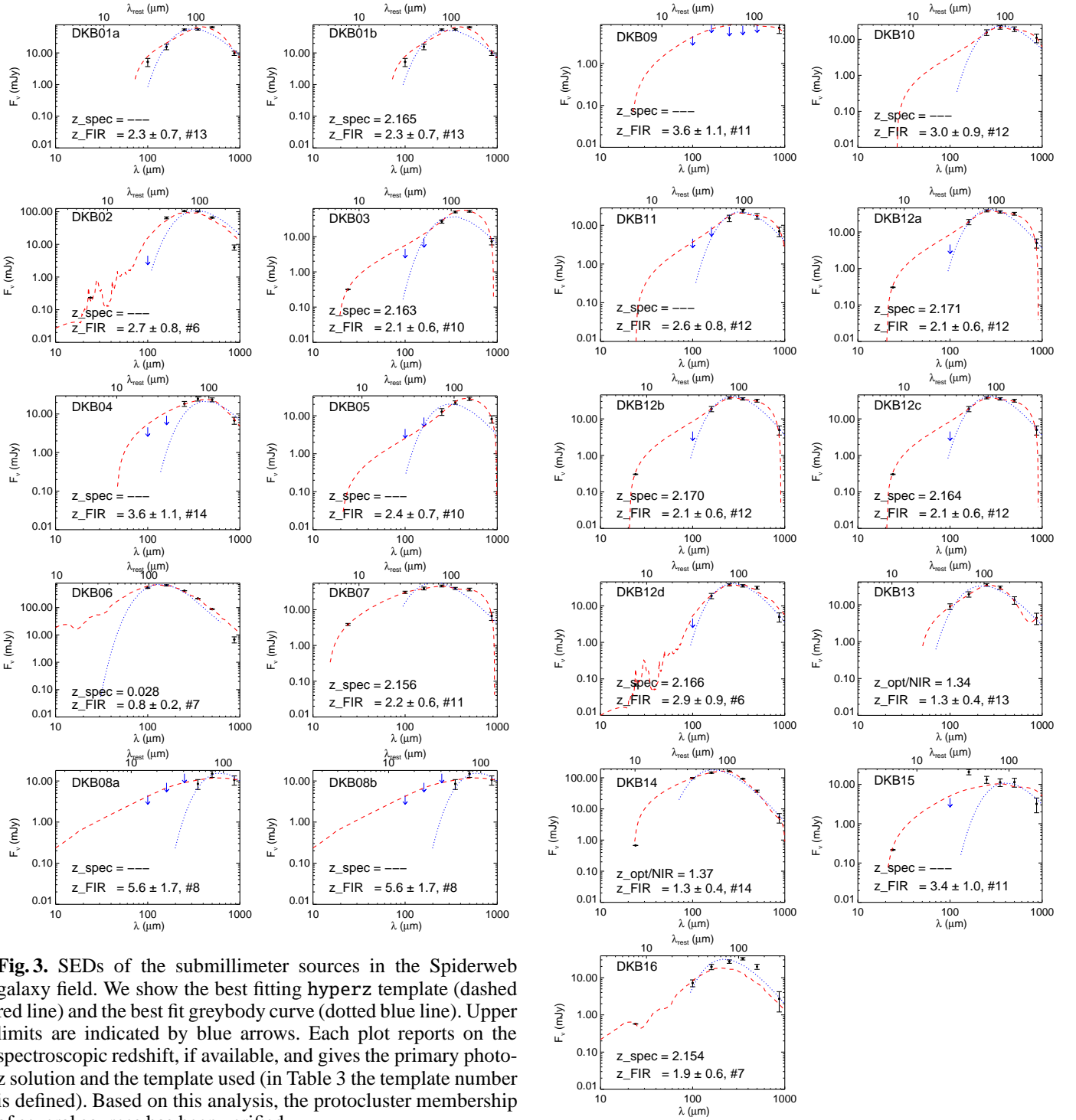


Fig. 3. SEDs of the submillimeter sources in the Spiderweb galaxy field. We show the best fitting hyperz template (dashed red line) and the best fit greybody curve (dotted blue line). Upper limits are indicated by blue arrows. Each plot reports on the spectroscopic redshift, if available, and gives the primary photo-z solution and the template used (in Table 3 the template number is defined). Based on this analysis, the protocluster membership of several sources has been verified.

e.g. DKB01, DKB07, DKB12b in Fig. 3. This is consistent with Seymour et al. (2012) who describe the contribution of the [CII] emission to the SPIRE 500 μm flux for MRC1138–262. See also Smail et al. (2011) for a detailed discussion of the effect of far-IR lines on far-IR/submm broad-band fluxes.

Fig. 5 shows the distribution of photometric redshifts for all 16 LABOCA sources. The results suggest that a significant fraction (about 50%) of the submillimeter sources are consistent with being protocluster members.

For sources with four or more detections in the *Herschel* and LABOCA bands we derive dust temperatures, far-IR luminosities and star formation rates (SFR), see Table 3. These sources

Fig. 3. (cont'd)

were fit with a grey-body law of the form: $S_\nu \propto \nu^\beta B_\nu(T_d) = \frac{\nu^{\beta+3}}{(e^{h\nu/kT_d} - 1)}$ where S_ν is the flux density at the rest-frame frequency ν , β the grain emissivity index and T_d the dust temperature. Dust temperatures for an interstellar medium only heated by star formation are expected to range between ~ 20 – 60 K, and β can range between 1–2.5 (Casey, 2012). For some sources spectroscopic redshift are known (Table 3) and we use them for the conversion to rest-frame flux density from which T_d and β are inferred through fitting. If no spectroscopic information is available, we use the photometric redshifts but also fix T_d to 35 K

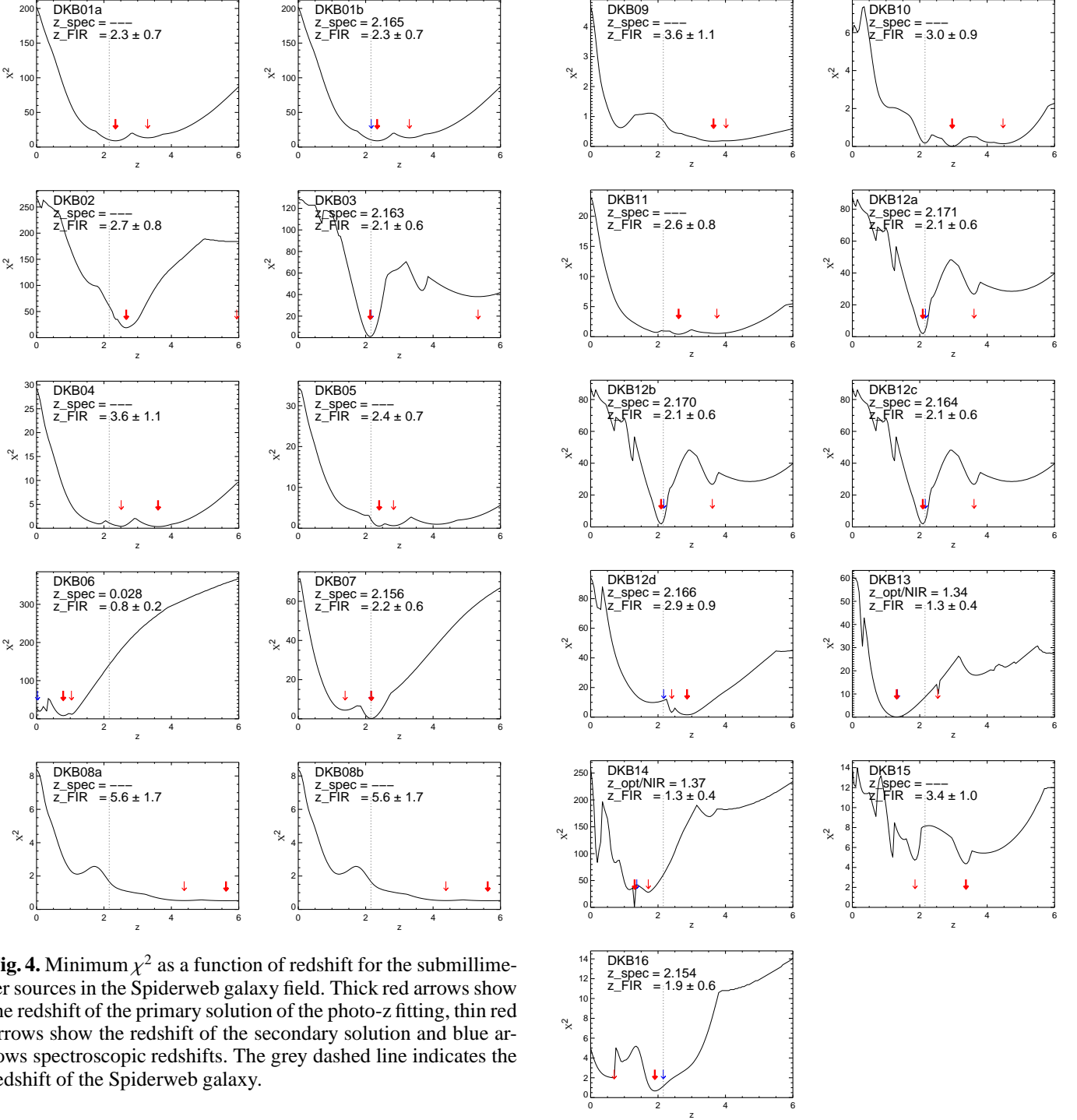


Fig. 4. Minimum χ^2 as a function of redshift for the submillimeter sources in the Spiderweb galaxy field. Thick red arrows show the redshift of the primary solution of the photo- z fitting, thin red arrows show the redshift of the secondary solution and blue arrows spectroscopic redshifts. The grey dashed line indicates the redshift of the Spiderweb galaxy.

and β to 1.5. This allows us to overcome the well known $T_d - z$ degeneracy (Blain et al., 2002). If only three detections in the far-IR are available, we also fix T_d and β and are thus able to estimate L_{far-IR} and SFR. Far-IR luminosities are derived by integrating the SED over the wavelength range 8 – 1000 μm and applying the relation $L_{FIR} = 4\pi D_L^2 F_{FIR}$ where D_L is the luminosity distance computed from their photometric redshifts (spectroscopic redshifts are used if they are available). We then estimate the star formation rates by using $SFR [M_\odot] = L_{FIR}/5.8 \times 10^9 L_\odot$ (Kennicutt, 1998)¹. The derived SFR of 1800 $M_\odot \text{ yr}^{-1}$ for

¹ We note that if we used the Chabier IMF (Chabrier, 2003) the SFRs would decrease by a factor of 1.8.

Fig. 4. (cont'd)

MRC1138–262 (DKB7) agrees well with the SFR found by Seymour et al. (2012).

5. Notes on individual objects

In this section we discuss secure and possible counterparts (based on the p-statistic) for all 16 LABOCA sources and whether the source could be a member of the large scale structure at redshift $z = 2.16$. SMG counterparts with spectroscopical confirmation at the redshift of the protocluster and consistent far-

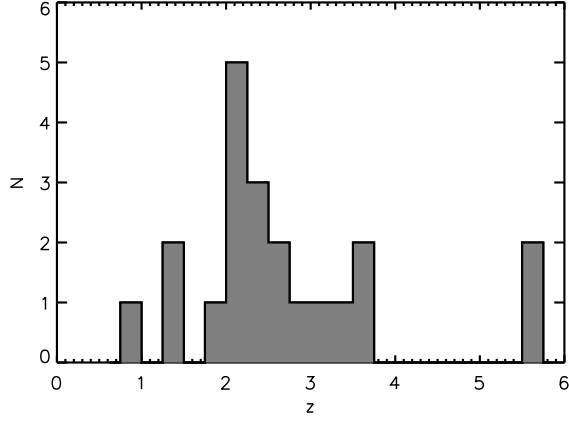


Fig. 5. Histogram of the far-infrared photometric redshifts (grey filled histogram). Our far-IR photometric analysis suggests that a significant fraction of the LABOCA sources are associated with the protocluster around the Spiderweb galaxy at $z = 2.2$.

IR photometric redshift are classified as secure members of this large scale structure at $z \approx 2.2$. We assess a protocluster membership as possible if the optical/near-infrared photometric redshift respectively the selection as an HAE without spectroscopic confirmation is strengthened by far-IR photo- z . We exclude the membership if optical/near-infrared and far-IR photo- z are discrepant. Remaining sources where no reliable judgement on the cluster membership can be made, we classify as uncertain members.

For each LABOCA source we show $40'' \times 40''$ images at radio, far-IR, $24\mu\text{m}$ and $\text{H}\alpha$ wavelengths (Fig. 6). We only discuss sources within the $9.5''$ search radius (the FWHM of the LABOCA beam). At redshift $z = 2.16$, 1 arcsec corresponds to 8.4 kpc.

'Secure' LABOCA sources

SMM J114100.0–263039 (DKB01, protocluster member YES) — There are two HAEs located $4''.5$ and $5''.7$ from the nominal LABOCA position. Both HAEs are classified as secure counterparts by the p-statistic and are only separated by $4''.5$ or 37.8 kpc. This counterpart has a spectroscopic redshift of 2.165 (Kurk et al. in prep.). The far-infrared photo- z $z_{\text{FIR}} = 2.3 \pm 0.7$ is consistent with the spectroscopic redshift. The association of *Herschel* flux with DKB01b strongly suggests that this source is (partly) responsible for the submillimeter emission. The closer HAE (DKB01a) has an optical/near-infrared photometric redshift of $z_{\text{opt/NIR}} = 2.84^{+0.05}_{-0.03}$ (Tanaka et al., 2010) and the redshift has been very recently confirmed to be $z = 2.2$ (Shimakawa et al., 2014). The *Herschel* detection appears to be associated to the more distant HAE, DKB01b. DKB01 and DKB03 are only separated by $24''.4$ (205 kpc) and the LABOCA map shown in Fig. 2 indicates that these two sources could be connected to each other.

SMM J114053.3–262913 (DKB02, (P)OSSIBLE MEMBER) — Within the LABOCA beam we find a prominent X-ray source: an AGN at $z = 1.512$ (X9 Pentericci et al., 2002; Croft et al., 2005). However, the secure VLA association ($5''.4$ away) is not associated with this X-ray source. The location of the *Herschel* PACS counterpart suggests that the LABOCA emission is related to the VLA source, $2''.4$ from the nominal LABOCA position, and not to the AGN at $z = 1.5$. No spec-

troscopic redshift is known for this radio source, but both the optical/near-infrared photometric redshift of $z_{\text{opt/NIR}} = 2.12^{+0.13}_{-0.20}$ (Tanaka et al., 2010) and the far-IR photometric redshift of $z_{\text{FIR}} = 2.7 \pm 0.8$ means this SMG is a plausible protocluster member. Finally, we note that $8''.2$ away from the nominal bolometric position lies an HAE candidate from the sample of Kurk et al. (# 211 in 2004a). Due to their shallower $\text{H}\alpha$ data Koyama et al. (2013a) do not recover this source. This source has no spectroscopic confirmation and lies $10''.4$ from the VLA position.

SMM J114058.3–263044 (DKB03, YES) — $7''.1$ away from the nominal LABOCA position we find a spectroscopically confirmed HAE ($z_{\text{spec}} = 2.163$; Kurk et al. in prep.) which is classified as secure by the corrected Poissonian probability. Neither VLA nor PACS counterparts are associated with this LABOCA source. However, DKB03 is detected at all three SPIRE wavelengths and the $z_{\text{FIR}} = 2.1 \pm 0.7$ is consistent with the spectroscopic redshift of the $\text{H}\alpha$ counterpart. The $250\mu\text{m}$ source position lies $9''.5$ from the nominal LABOCA position, but only $3''.4$ from the confirmed $\text{H}\alpha$ emitter, suggesting that this near-infrared excess source emits (some of) the dust emission detected by LABOCA.

SMM J114046.8–262539 (DKB04, (U)NKNOWN) — This source is only covered by the *Herschel* and VLA imaging. A faint, secure, 3.3σ VLA counterpart, not detected by *Herschel*, lies $7''.0$ from the nominal LABOCA position.

SMM J114043.9–262340 (DKB05, U) — Only *Herschel* and VLA coverage exist of this 4.5σ LABOCA detection. A *Herschel* source detected at all three SPIRE bands is associated with this SMG.

SMM J114059.5–263200 (DKB06, NO) — At the position of this SMG, we find a local spiral galaxy at $z = 0.028$ (Jones et al., 2009). A $121.7\mu\text{Jy}$ faint radio source lies $5''.9$ from the nominal bolometer position. This VLA counterpart is detected by the Chandra X-ray Observatory (X14 in Pentericci et al., 2002). Within the LABOCA beam two more X-ray sources are found by the same authors (X13 and X15). According to Pentericci et al. (2002) all three sources are related to the spiral galaxy. The spiral galaxy is also detected at two IRAS bands, at 60 and $100\mu\text{m}$ (IRAS F11384–2615; Moshir & et al., 1990). Based on the IRAS colours (Perault et al., 1987) we estimate an infrared luminosity $L_{\text{IR}} = 4.1 \times 10^8 L_{\odot}$. The PACS flux measured at $100\mu\text{m}$ of $530.9 \pm 26.6\text{ mJy}$ is lower than the IRAS flux of $790 \pm 180\text{ mJy}$ at the same wavelength. The VLA counterpart is detected at PACS wavelengths as well. This source is the brightest object in the *Herschel* images. As far as we know this object is one of the lowest redshift SMGs discovered by blind submillimeter ground based surveys. Only a handful of SMGs in the local Universe are known (e.g., Webb et al., 2003a; Chapman et al., 2005). However the submillimeter source may lie behind the spiral galaxy. The far-infrared photometric redshift discussed in Section 4 suggests $z_{\text{FIR}} = 0.8 \pm 0.2$, however, the χ^2 distribution shown in Fig. 4 indicates lower redshift solutions are also plausible. PACS would not be able to detect the very low infrared luminosity of $L_{\text{IR}} = 8.6 \times 10^9 L_{\odot}$ if it was emitted at $z \approx 1$. Furthermore, due the sensitivity of the IRAS satellite, the IRAS flux can only be associated to the spiral galaxy.

SMM J114048.4–262914 (DKB07, YES) — Seymour et al. (2012) discuss in detail the infrared properties of this radio galaxy, MRC1138–262. The LABOCA detection seems to be slightly elongated, which is also seen in the SPIRE bands at 350 and 500 μm (Seymour et al., 2012) and in SCUBA 850 μm data (Stevens et al., 2003), see also section 6.1 for more details. This feature may be well due to multiple sources blended together, see also e.g., Karim et al. (2013) and Hodge et al. (2013) for details on this topic.

SMM J114033.9–263125 (DKB08, U) — Within the LABOCA beam we find two promising counterparts. The secure VLA source (DKB08b; $S_{1.4\text{ GHz}} = 70.9 \pm 19.0\ \mu\text{Jy}$) lies at the edge of the LABOCA beam (8'5 from the nominal bolometer position). At a distance of 5'4 from the LABOCA position, lies a bright *Herschel* H α emitter. Unfortunately, no optical/NIR photo-z exists for these sources.

SMM J114040.9–262555 (DKB09, U) — This LABOCA source is undetected at VLA and *Herschel* wavelengths and is not covered by H α imaging.

SMM J114043.7–262216 (DKB10, U) — This is our brightest LABOCA source ($S_{870\ \mu\text{m}} = 11.0 \pm 3.0\ \text{mJy}$), located at the edge and thus at the noisiest part of our LABOCA map. It is the only SMG without PACS coverage. The reliability of the LABOCA detection is strengthened by a SPIRE source which is 8'1 separated from the nominal LABOCA position and peaks at 350 μm .

SMM J114038.5–263201 (DKB11, U) — At the edge of the LABOCA beam, 8'0 away from the nominal LABOCA position, we find a 350 μm peaker which could lie at $z = 2.6 \pm 0.7$. Only 4'3 from the LABOCA position lies a candidate Ly α emitter (#73 in Kurk et al., 2004a). However, Croft et al. (2005) reveal a spectroscopic redshift of 0.671 for this source.

SMM J114057.6–262933 (DKB12, YES) — This 3.6σ LABOCA detection is the most complex source in our sample. A 162.7 μJy bright 20 cm source lies 3'2 away from the nominal LABOCA position. Four HAEs, separated by only 5'5 (46.2 kpc) lie within the LABOCA beam. Two emitters show a strong H α line at $z = 2.170$ (DKB12a) and $z = 2.163$ (DKB12c) in ISAAC spectroscopy (Kurk et al. in prep.). SINFONI 3D spectroscopy of this complex source confirms that the components 12b (VLA counterpart) and 12d lie at similar redshifts. From the SINFONI observations we obtain following spectroscopic redshifts: 12a: $z = 2.171$, 12b: $z = 2.170$, 12c: $z = 2.164$, and 12d: $z = 2.166$ (Kurk et al., in prep.). The latter source is also selected as a Ly α emitting candidate (Kurk et al., 2004a). The PACS beam has a FWHM of 6'0 at 100 μm so it is impossible to associate the *Herschel* fluxes to one or more of these components directly. Millimeter interferometric observations are crucial in order to reveal the locations of the dust emission within this complex.

'Cross-identified tentative' LABOCA sources

SMM J114048.3–262748 (DKB13, NO) — We find a secure 20 cm radio source 6'0 away from the nominal LABOCA position. The radio source seems to be associated with *Herschel* detections at all five bands. However, the *Herschel* SPIRE colours exclude protocluster membership and favour a lower redshift. This finding is consistent with the derived optical/NIR

photometric redshift of $z_{\text{opt/NIR}} = 1.34^{+0.10}_{-0.07}$ (Tanaka et al., 2010) for the VLA source.

SMM J114042.4–262715 (DKB14, NO) — Only 1'8 away from the nominal LABOCA position lies the brightest radio counterpart (618.5 μJy) of an SMG in our sample. This VLA source is detected by *Herschel* at all five bands. Again the *Herschel* colours imply a low redshift. The optical-NIR counterpart photometric redshift suggests $z_{\text{opt/NIR}} = 1.37^{+0.08}_{-0.07}$ (Tanaka et al., 2010). Both redshift estimates exclude DKB14 from being a protocluster member.

SMM J114054.3–262800 (DKB15, P) — 7'4 away from the nominal LABOCA position we find a tentative HAE association with $z_{\text{opt/NIR}} = 2.60^{+0.24}_{-0.24}$. We detect two PACS 160 μm counterparts (one classified as secure and the other is not secure) that are separated by only 11'2, which are undetected at PACS 100 μm . The secure PACS 160 μm counterpart seems to be physically associated with the HAE. No other SMG in our sample has two PACS counterparts and no such system was seen in GOODS-N (Dannerbauer et al., 2010). At the edge of the PACS 160 μm beams, we find the candidate Ly α emitters L877 (Kurk et al., 2004a). However, this LAE lies at $z_{\text{spec}} = 0.863$ (Croft et al., 2005). The far-IR photometric analysis (Fig. 3) does not exclude $z = 2.2$ as a possible far-IR photometric redshift for the HAE.

SMM J114102.7–262746 (DKB16, YES) — This source has a wide multiwavelength coverage. Pentericci et al. (2002) report X-ray emission for this source (X16), Kurk et al. (2004a) selected this source as LAE candidate (L778) and it is detected at 1.4 GHz. Subsequent rest-frame UV-spectroscopy by Croft et al. (2005) reveal both the redshift $z_{\text{spec}} = 2.149$ and the AGN nature of this source. An H α line was detected at $z = 2.154$ by Kurk et al. (in prep) and the width of the H α line is consistent with the AGN nature of this source. The velocity offset between the Ly α and H α line is +476 km s $^{-1}$ which is typical for LAEs and LBGs (Shapley et al., 2003) indicating gas outflow from this source.

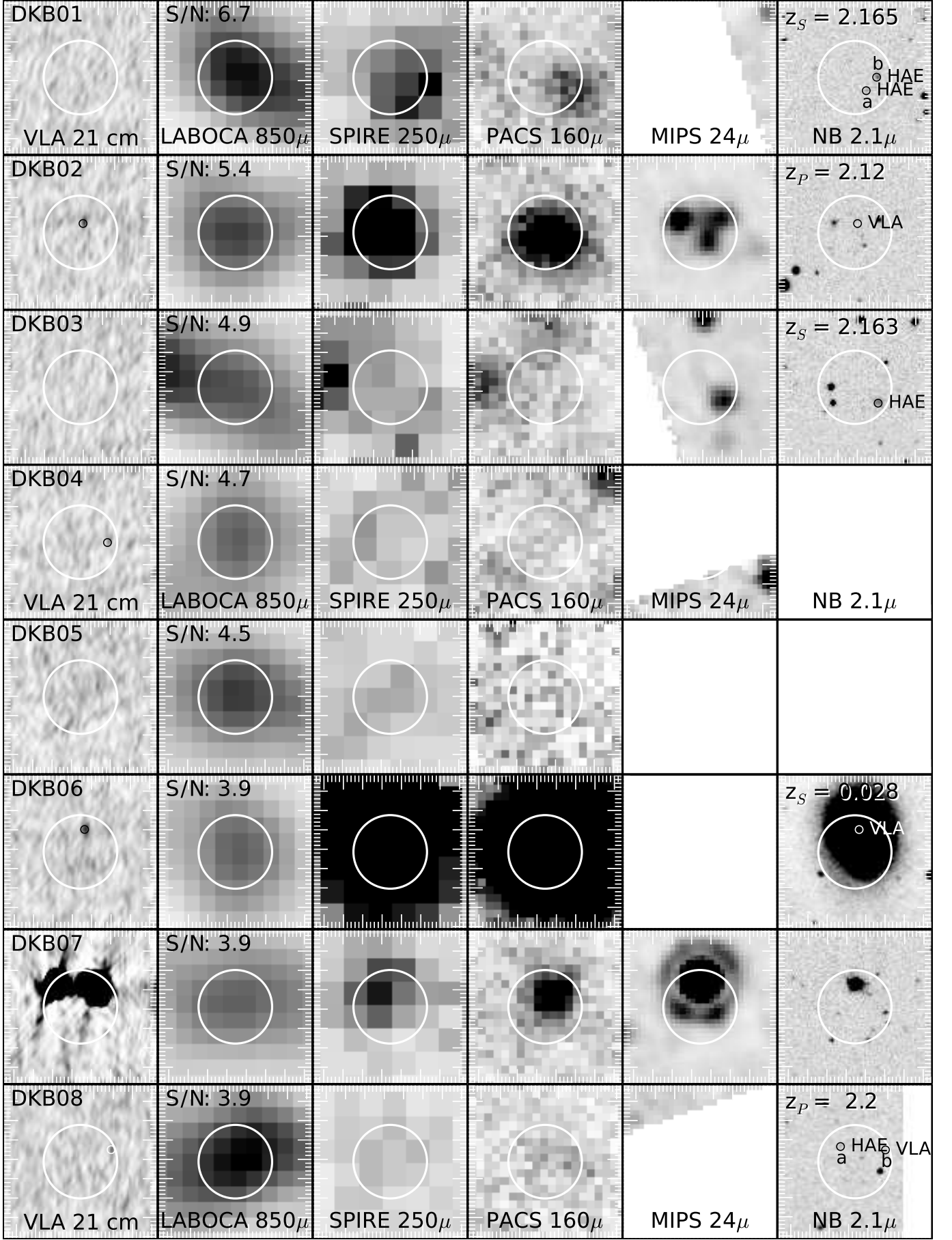


Fig. 6. Postage stamps of all 16 LABOCA sources, including VLA 1.4 GHz, LABOCA 870 μ m, SPIRE 250 μ m, PACS 160 μ m, MIPS 24 μ m and MOIRCS $z = 2.16$ H α images. The 40'' \times 40'' images are centered on the nominal LABOCA position and orientated such that north is at the top and east is to the left. The large white circle represents the size of the LABOCA beam ($\sim 19''$ diameter). Small circles are VLA and/or HAE sources. Spectroscopic (S) and photometric (P) redshifts are labeled in the top of the H α images.

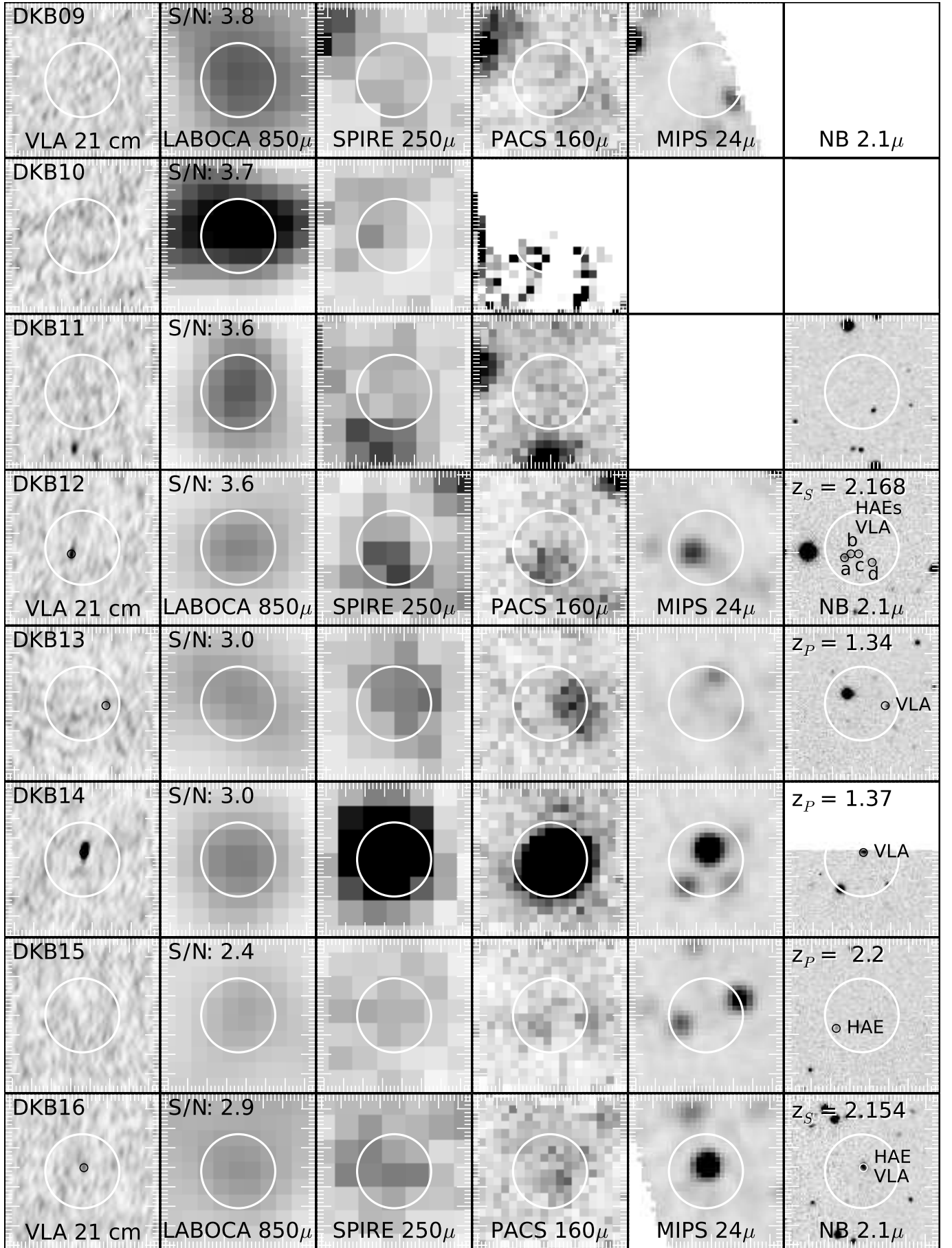


Fig. 6. (cont'd)

Table 2. Main properties of counterparts of the 870 μm LABOCA sources in the field around MRC1138–256

Source (IAU) (1)	Alias (2)	R.A. (J2000) (3)	Decl. (J2000) (4)	Separation (arcsec) (5)	$z_{\text{opt/NIR}}$ (6)	$S_{24\mu\text{m}}$ (μJy) (7)	$S_{100\mu\text{m}}$ (mJy) (8)	$S_{160\mu\text{m}}$ (mJy) (9)	$S_{250\mu\text{m}}$ (mJy) (10)	$S_{350\mu\text{m}}$ (mJy) (11)	$S_{500\mu\text{m}}$ (mJy) (12)	$S_{870\mu\text{m}}$ (mJy) (13)	$S_{1.4\text{GHz}}$ (μJy) (14)	Counterpart (15)
SMM 114100.0–263039	DKB01a	11:40:59.82	–26:30:42.6	4.5	$2.84^{+0.05}_{-0.03}$...	5.2 ± 1.5	15.7 ± 3.1	54.4 ± 2.7	55.2 ± 2.7	64.5 ± 2.6	9.8 ± 1.5	< 57.0	HAE
SMM 114100.0–263039	DKB01b	11:40:59.62	–26:30:39.1	5.7	2.165^*	...	5.2 ± 1.5	15.7 ± 3.1	54.4 ± 2.7	55.2 ± 2.7	64.5 ± 2.6	9.8 ± 1.5	< 57.0	HAE
SMM 114053.3–262913	DKB02	11:40:53.23	–26:29:11.7	2.4	$2.12^{+0.13}_{-0.20}$	232.6 ± 5.0	< 4.5	65.0 ± 4.4	104.4 ± 3.1	101.9 ± 2.7	66.4 ± 3.0	8.1 ± 1.5	123.2 ± 19.0	VLA
SMM 114058.3–263044	DKB03	11:40:57.81	–26:30:48.1	7.2	2.163^*	316.9 ± 5.0	< 4.5	< 9.0	26.8 ± 2.8	49.9 ± 2.7	52.1 ± 2.8	7.3 ± 1.5	< 57.0	HAE
SMM 114046.8–262539	DKB04	11:40:46.23	–26:25:39.3	7.0	< 4.5	< 9.0	18.4 ± 2.7	24.6 ± 3.0	23.4 ± 2.7	6.8 ± 1.4	63.0 ± 19.0	VLA
SMM 114043.9–262340	DKB05	< 4.5	< 9.0	12.8 ± 2.6	22.4 ± 2.3	27.9 ± 2.7	8.2 ± 1.8	< 57.0	...
SMM 114059.5–263200	DKB06	11:40:59.46	–26:31:54.9	5.9	0.028°	...	530.9 ± 26.6	652.0 ± 32.7	413.8 ± 3.1	214.9 ± 2.7	87.7 ± 3.1	6.8 ± 1.7	121.7 ± 19.0	VLA
SMM 114048.4–262914	DKB07	2.160^\dagger	3890.0 ± 250.0	30.7 ± 2.2	42.3 ± 3.0	46.1 ± 2.8	39.5 ± 2.6	36.8 ± 3.2	6.7 ± 1.7	8710 ± 35	HzRG (HAE , $2 \times \text{HAE}$)
SMM 114033.9–263125	DKB08a	11:40:34.16	–26:31:21.7	5.4	2.2	...	< 4.5	< 9.0	< 15.0	8.5 ± 2.3	15.0 ± 2.8	10.6 ± 2.7	< 57.0	HAE
SMM 114033.9–263125	DKB08b	11:40:33.29	–26:31:22.5	8.5	< 4.5	< 9.0	< 15.0	8.5 ± 2.3	15.0 ± 2.8	10.6 ± 2.7	70.9 ± 19.0	VLA
SMM 114040.9–262555	DKB09	< 4.5	< 9.0	< 7.5	< 8.0	< 9.0	7.1 ± 1.9	< 57.0	...
SMM 114043.7–262216	DKB10	15.6 ± 2.8	21.5 ± 2.4	19.3 ± 2.9	11.0 ± 3.0	< 57.0	...
SMM 114038.5–263201	DKB11	< 4.5	< 9.0	15.3 ± 2.9	23.4 ± 2.5	17.3 ± 2.8	7.0 ± 1.9	< 57.0	...
SMM 114057.6–262933	DKB12a	11:40:57.91	–26:29:36.3	5.2	2.171^*	303.4 ± 5.0	< 4.5	18.8 ± 3.1	37.8 ± 2.5	35.4 ± 2.7	31.5 ± 2.8	5.0 ± 1.4	< 57.0	HAE
SMM 114057.6–262933	DKB12b	11:40:57.79	–26:29:35.3	3.2	2.170^*	303.4 ± 5.0	< 4.5	18.8 ± 3.1	37.8 ± 2.5	35.4 ± 2.7	31.5 ± 2.8	5.0 ± 1.4	162.7 ± 19.0	VLA*, HAE
SMM 114057.6–262933	DKB12c	11:40:57.64	–26:29:35.3	1.8	2.164^*	303.4 ± 5.0	< 4.5	18.8 ± 3.1	37.8 ± 2.5	35.4 ± 2.7	31.5 ± 2.8	5.0 ± 1.4	< 57.0	HAE
SMM 114057.6–262933	DKB12d	11:40:57.38	–26:29:37.5	4.7	2.166^*	68.5 ± 5.0	< 4.5	18.8 ± 3.1	37.8 ± 2.5	35.4 ± 2.7	31.5 ± 2.8	5.0 ± 1.4	< 57.0	HAE
SMM 114048.3–262748	DKB13	11:40:47.89	–26:27:48.5	6.1	1.34^*	< 15.0	9.0 ± 1.6	19.3 ± 3.2	34.8 ± 2.7	29.2 ± 2.9	13.4 ± 3.1	4.4 ± 1.5	93.7 ± 19.0	VLA
SMM 114042.4–262715	DKB14	11:40:42.35	–26:27:13.7	1.8	1.37^*	672.4 ± 5.0	97.4 ± 5.1	146.1 ± 7.9	161.0 ± 2.9	92.7 ± 2.6	37.1 ± 3.0	5.3 ± 1.8	618.5 ± 19.0	VLA
SMM 114054.5–262800	DKB15	11:40:54.75	–26:28:03.4	7.4	2.2	216.7 ± 5.0	< 4.5	20.7 ± 3.2	13.3 ± 2.7	11.3 ± 2.5	11.4 ± 2.9	3.2 ± 1.3	< 57.0	HAE
SMM 114102.7–262746	DKB16	11:41:02.38	–26:27:45.1	1.0	$2.154^{*\ddagger}$	572.1 ± 5.0	7.2 ± 1.5	19.6 ± 3.2	27.1 ± 2.9	32.2 ± 2.4	19.8 ± 3.1	4.2 ± 1.4	76.2 ± 19.0	HAE**, VLA

Notes. — Col. (1): LABOCA source. Col. (2): Short name of LABOCA source. Col. (3-4): J2000.0 coordinates of associated LABOCA counterparts either from VLA or H α observations. Col. (5): Separation between nominal LABOCA bolometer and counterpart position. Col. (6): Spectroscopic (three digits after the decimal), photometric redshift (two digits after the decimal) and H α imaging (one digit after the decimal) of the LABOCA counterpart. *: Kurk et al. in prep.; $^\circ$: Jones et al. (2009); † : Kuiper et al. (2011); $^\bullet$: Tanaka et al. (2010). ‡ : Previously, Croft et al. (2005) obtained a rest-frame UV-spectroscopic redshift of $z = 2.149$ for the counterpart of DKB16. Col. (7-14): Flux measurements with *Spitzer*, *Herschel*, LABOCA and VLA. For multiple component counterparts as DKB01, DKB08 and DKB12, we give for the individual components the *Spitzer* and *Herschel* fluxes associated to the LABOCA detection. For the *Herschel* bands we give source detection errors. In case of the VLA measurements, we list the peak flux. Col. (15): Type of LABOCA counterpart. Secure counterparts are in bold face. *: In case of DKB12b we list the VLA position. **: In case of DKB16 we list the HAE position.

H. Dannerbauer et al.: APEX LABOCA observations of the field around MRC1138–262

6. Characteristics of the LABOCA overdensity

6.1. Previous SCUBA observations

Stevens et al. (2003) observed a small field of $\sim 2'$ diameter centered on MRC1138–262 with SCUBA and report four detections including the radio galaxy. They reported a higher source density than expected from blank fields (by one source). However, we only recover two of these sources with our LABOCA observations, which are at a very similar wavelength to the SCUBA observations. The other two SCUBA sources are fainter ($S_{850\mu\text{m}}=3.1$ and 2.2 mJy) than the 3σ detection limit of ~ 4 mJy at this part of our LABOCA map. The fluxes of our two LABOCA sources, the radio galaxy and DKB02, are consistent with the ones obtained from the SCUBA observations. In addition, we do not find the proposed alignment between HzRG radio axis and bright submillimeter companions.

However, similar to Stevens et al. (2003), we find that the LABOCA emission of MRC1138–262 is spatially extended. Seymour et al. (2012) find that this extension consists of four galaxies detected by *Spitzer*, two of them are spectroscopically identified to lie at the same redshift (Kurk et al., 2004b), cf. with Ivison et al. (2008, 2012). $30''$ west of the radio galaxy,

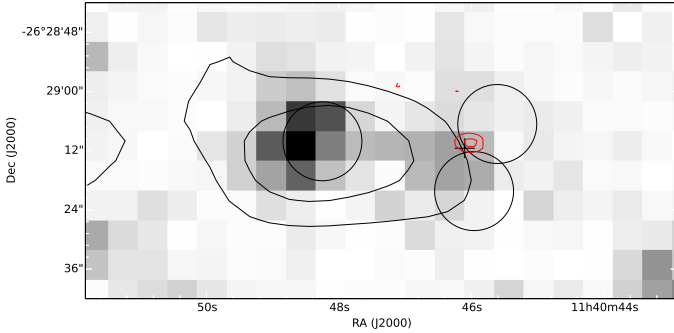


Fig. 7. Environment of the radio galaxy MRC1138. SPIRE $250\mu\text{m}$ is shown in greyscale. The black contours are the (extended) LABOCA emission of the radio galaxy, indicating levels at 2.0, 4.0 and 6.0 mJy/beam. The circles with a diameter of $16''$ (the FWHM of SCUBA) indicate SCUBA emission (Stevens et al., 2003). The red contours show the location of the CO(1-0) emission (Emonts et al., 2013) associated to the spectroscopically confirmed H α emitter # 229 at $z = 2.15$ (Kurk et al., 2004b). The CO levels are 0.134 and 0.168 mJy/beam.

Emonts et al. (2013) report CO(1-0) emission at 3.7σ significance associated with the spectroscopically confirmed H α emitter #229 at $z = 2.149$ (Kurk et al., 2004b) — Koyama et al. (2013a) also select this source as H α emitter. This cold molecular gas reservoir is now confirmed through very recent ATCA observations (Emonts, priv. communication). This CO-bright HAE lies $8.1''$ south-east away from the nominal SCUBA position of source # 3 (Stevens et al., 2003), see Fig. 7. Below the published SCUBA source, we see dust emission at low level in the SCUBA map (see Fig. 1 in Stevens et al., 2003). SPIRE emission, coincident with the position of HAE229, lies in between the northern and southern components and seems to be related to the extended LABOCA emission of the HzRG. We speculate that the northern and southern components are one submm source but due to the chopper throw used in the SCUBA observations, negative flux from the central HzRG was added right

Table 4. Fluxes of the CO-bright H α emitter #229

Band (1)	Flux (2)	Unit (3)	Instrument (4)
$S_{24\mu\text{m}}$	477.4 ± 5.0	μJy	MIPS
$S_{100\mu\text{m}}$	< 4.5	mJy	PACS
$S_{160\mu\text{m}}$	13.6 ± 4.0	mJy	PACS
$S_{250\mu\text{m}}$	26.0 ± 2.8	mJy	SPIRE
$S_{350\mu\text{m}}$	27.2 ± 2.9	mJy	SPIRE
$S_{500\mu\text{m}}$	26.5 ± 2.7	mJy	SPIRE
$S_{850\mu\text{m}}$	2.2 ± 1.4	mJy	SCUBA

Notes. — Col. (1): Band in which flux is measured. Col. (2): Units of the flux density measurements. Limit of PACS $100\mu\text{m}$ observation is 3σ . Col (3): Our measurements for HAE229. SCUBA flux is from Stevens et al. (2003). Col. (4): Instruments.

on the source, cutting it into two and artificially reducing the total flux. HAE229 is detected at PACS $160\mu\text{m}$ and at all three SPIRE bands (see Table 4) and we derive a far-IR photometric redshift $z_{\text{FIR}} = 1.8 \pm 0.5$ assuming the total SCUBA flux of SCUBA source #3 is $S_{850\mu\text{m}} = 2.2 \pm 1.4$ mJy (Stevens et al., 2003). However, we note that the true amount of submm emission at $850\mu\text{m}$ is uncertain and only deeper and higher resolution observations will reveal the true configuration of this source in the submm window. We conclude that the CO-bright HAE229 is an SMG related to the protocluster at $z \approx 2.2$. However, as this source is not detected by our LABOCA observations as a single source we will exclude it in the forthcoming discussion. The extended LABOCA emission of MRC1138–262 suggests that most probably, the LABOCA emission of HAE229 is blended with the one of the radio galaxy.

6.2. Ly α emitting counterparts to LABOCA sources

Besides MRC1138–262, three SMGs (DKB12, DKB15 and DKB16) are associated with LAEs. In two cases (DKB12d and DKB16), the LAE has been confirmed by H α spectroscopy (Kurk et al., in prep.). This result is in contrast to the work by De Breuck et al. (2004) on the protocluster around the $z = 4.1$ radio galaxy TN J1338–1942 who reported no associations of confirmed LAEs with SMGs. However, this discrepancy could be explained thereby that both LAEs have been selected as HAEs (Koyama et al., 2013a) and DKB12 is even seen at PACS wavelengths (cf. Oteo et al., 2012, PACS detection of 2/72 LAEs between $z = 2.0 - 3.5$).

6.3. H α emitting counterparts to LABOCA sources

As discussed in Section 3.4 we find six out of 11 SMGs covered by H α imaging at $z \approx 2.2$ are associated with HAEs. We search the literature for H α surveys of fields containing SMGs at the redshift of the survey and find H α narrow band observations of the SSA 13 field at $z \approx 2.23$, which included two SMGs at the probed redshift range (Matsuda et al., 2011). None of the two SMGs were selected as HAEs with fluxes greater than $f(\text{H}\alpha) \approx 1.0 \cdot 10^{-16} \text{ erg s}^{-1} \text{ cm}^{-2}$. The flux limit of the Koyama et al. (2013a) data is $f(\text{H}\alpha) \approx 3.0 \cdot 10^{-17} \text{ erg s}^{-1} \text{ cm}^{-2}$. Approximately 50% of the HAEs associated to SMGs in the MRC 1138-262 field would be missed if the Koyama et al. (2013a) H α images were of a similar depth to the Matsuda et al. (2011) data.

All SMGs with HAEs counterparts beside one (DKB16) have a large discrepancy between the SFR derived from H α and

Table 3. Redshifts, star formation rates and results of the far-IR SED fitting of the 870 μm LABOCA sources in the field around MRC1138–256

Alias	Member	$z_{\text{opt/NIR}}$	z_{FIR}	$\text{SFR}_{\text{H}\alpha}$ ($\text{M}_{\odot} \text{ yr}^{-1}$)	SFR_{FIR} ($\text{M}_{\odot} \text{ yr}^{-1}$)	L_{FIR} ($10^{12} L_{\odot}$)	T (K)	β	Template
(1)	(2)	(3)	(4)	(5)	(6)	(7)	(8)	(9)	(10)
DKB01a	YES	$2.84^{+0.05}_{-0.03}$	2.3 ± 0.7	30	1320	7.6	35	1.5	#13 (DKB13)
DKB01b	YES	2.165	2.3 ± 0.7	230	1090	6.3	37	1.3	#13 (DKB13)
DKB02	P	$2.12^{+0.13}_{-0.20}$	2.7 ± 0.8		3080	17.9	35	1.5	#6 (I22491)
DKB03	YES	2.163	2.1 ± 0.6	290	650	3.8	31	1.5	#10 (DKB03)
DKB04	U	...	3.6 ± 1.1		1010	5.9	35	1.5	#14 (DKB14)
DKB05	U	...	2.4 ± 0.7		490	2.8	35	1.5	#10 (DKB03)
DKB06	NO	0.028	0.8 ± 0.2		1	0.009	22	1.9	#7 (Mrk231)
DKB07	YES	2.160	2.2 ± 0.6		1750	10.1	56	1.0	#11 (DKB07)
DKB08a	U	2.2	5.6 ± 1.7	>20*	1460	8.4	35	1.5	#8 (QSO1)
DKB08b	U	..	5.6 ± 1.7		1460	8.4	35	1.5	#8 (QSO1)
DKB09	U	...	3.6 ± 1.1		†	†	†	†	#11 (DKB07)
DKB10	U	...	3.0 ± 0.9		810	4.7	35	1.5	#12 (DKB12c)
DKB11	U	...	2.6 ± 0.8		620	3.6	35	1.5	#12 (DKB12c)
DKB12a	YES	2.171	2.1 ± 0.6	240	860	5.0	35	1.8	#12 (DKB12c)
DKB12b	YES	2.170	2.1 ± 0.6	160	860	5.0	35	1.8	#12 (DKB12c)
DKB12c	YES	2.164	2.1 ± 0.6	30	850	4.9	35	1.8	#12 (DKB12c)
DKB12d	YES	2.166	2.9 ± 0.9	100	850	4.9	35	1.8	#6 (I22491)
DKB13	NO	$1.34^{+0.10}_{-0.07}$	1.3 ± 0.4		280	1.6	38	1.0	#13 (DKB13)
DKB14	NO	$1.37^{+0.08}_{-0.07}$	1.3 ± 0.4		2020	11.7	45	1.6	#14 (DKB14)
DKB15	P	2.2	3.4 ± 1.0	90	460	2.7	35	1.5	#11 (DKB07)
DKB16	YES	2.154	1.9 ± 0.6	1140	830	4.8	48	1.3	#7 (Mrk231)

Notes. — Col. (1): Short name of LABOCA source. Col. (2): Classification on membership of the $z \approx 2.2$ protocluster structure. YES=secure member; P=possible member; U=no reliable statement on membership could be made; NO=membership securely excluded. Col. (3): Spectroscopic (three digits after the decimal), photometric redshift (two digits after the decimal) and $\text{H}\alpha$ imaging (one digit after the decimal) of the LABOCA counterpart. Col. (4): Redshift estimate from the far-infrared SED. Col. (5): The star formation rate derived from narrow-band $\text{H}\alpha$ imaging (Koyama et al., 2013a) is based on the NB flux and includes corrections for [NII] contamination and dust extinction following Koyama et al. (2013a). *: Due to its faintness in the K_s -band no corrections could be applied. Col. (6): Star formation rate derived from our infrared luminosities estimates and using the conversion from Kennicutt (1998). Col. (7): Far-infrared Luminosity. Col. (8): Dust Temperature. Col. (9): Spectral index. In order to overcome the well-known $T - z$ degeneracy (e.g., Blain et al., 2002), we fixed the temperature T to 35 K and the spectral index β to 1.5 where no spectroscopic information is available. The same we also do for sources with only 3 detections in the far-IR bands. Col. (10): Template used.

†: DKB09 is only detected at 870 μm , therefore no physical properties are derived.

from the far-IR indicating these sources are highly dust-obscured (consistent with Swinbank et al., 2004). It may demonstrate that a large amount of star formation activity is missed when using the $\text{H}\alpha$ line as a SFR indicator (see also Koyama et al., 2010). The $\text{H}\alpha$ derived SFR (based on the narrow-band imaging by Koyama et al. (2013a) and corrected for [NII] contamination and dust extinction following Koyama et al. (2013a)) ranges between ~ 30 to $300 \text{ M}_{\odot} \text{ yr}^{-1}$ for all beside one source (DKB16, $\text{SFR}_{\text{H}\alpha}=1140 \text{ M}_{\odot} \text{ yr}^{-1}$) whereas the SFR derived from our IR observations ranges between 300 to $1800 \text{ M}_{\odot} \text{ yr}^{-1}$.

In Fig. 8, we investigate the relation between the stellar mass (derived from rest-frame R-band magnitudes, see Koyama et al., 2013a, for more details) and the star formation rate (derived from the $\text{H}\alpha$ line) for the complete sample of HAEs discovered in the field of MRC1138–262. In addition, we show the location of HAEs counterparts of LABOCA sources that are protocluster members. There seems to be a weak trend that the HAEs associated with LABOCA sources are more massive and have higher SFRs than the overall population of HAEs in the field of the radio galaxy. In addition, we derive SFRs based on the far-IR measurements for LABOCA sources selected as HAEs and reveal that these sources (far-IR bright HAEs) are off the star-formation main sequence for $z \sim 2$ galaxies (Daddi et al., 2007; Santini et al., 2009).

6.4. Large scale structure traced by SMGs at $z = 2.2$

We compare the number counts of the MRC1138–262 field with APEX LABOCA blank field observations of the LESS survey (Weiß et al., 2009), extracting sources with a significance level above 3.7σ (the extraction limit of the LESS survey) in our data. We detect six sources with at least 3.7σ and fluxes greater than 7.0 mJy in our map (DKB01, DKB02, DKB03, DKB05, DKB09, DKB11). The size of the map with a maximum noise of 1.9 mJy is 56 arcmin^2 , yielding an estimated surface density of $0.107 \text{ arcmin}^{-2}$. According to the number counts derived by Weiß et al. (2009), we expect a surface density down to the flux level of 7 mJy of $0.028 \text{ arcmin}^{-2}$. However, we should take into account the fact that the LESS field could be underdense compared to previous submm surveys (e.g., Weiß et al., 2009; Wardlow et al., 2011) down to $S_{850 \mu\text{m}} \gtrsim 3 \text{ mJy}$ by a factor of two. Thus the source density in the MRC1138–262 field is approximately two (to four) times higher than expected.

We compare the differential source counts for our sources with $S_{850 \mu\text{m}} \gtrsim 7 \text{ mJy}$ to those in the ECDFS (Weiß et al., 2009) and corrected (multiplied) by the ‘underdense factor’ of two (see Swinbank et al., 2014, for this approach). We find that we can fit the differential source counts in our field very well with the curves fitted to the ECDFS counts, as provided by Weiß et al. (2009), normalised by a factor 3.8. This implies that over the (small) range of source fluxes probed by our map, we consis-

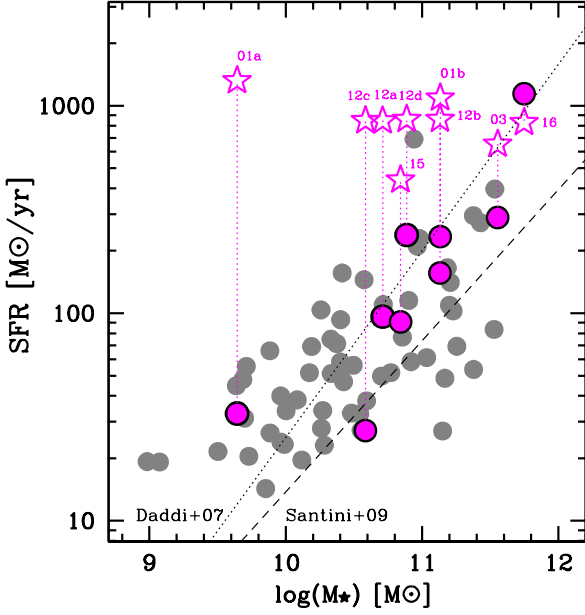


Fig. 8. Stellar mass vs. star formation rate (derived from the $H\alpha$ line) for the complete sample of $H\alpha$ emitters (grey dots) discovered in the field of MRC1138–262 (Koyama et al., 2013a). Only DKB07 and DKB08a are excluded as the estimates of the stellar mass of the associated HAEs are unreliable. The pink dots indicate the $H\alpha$ emitters located within the LABOCA beam aperture for all LABOCA source. The SFR based on the far-IR measurements is shown as open pink stars (connected with dotted lines). The far-IR measurements reveal that far-IR bright HAEs (LABOCA sources) are off the star-formation main sequence for $z \sim 2$ galaxies (Daddi et al., 2007; Santini et al., 2009).

tently find a 3.8 times higher density as compared to a blank field.

To understand how unusual the collection of SMGs found in the field of MRC1138–262 is, we compared it with the spatial distribution of sources in the ECDFS (Weiß et al., 2009). We count the number of $S_{850} > 7$ mJy sources within 10,000 randomly placed circles each having a radius of $4.22'$ (i.e., an area of 56 arcmin^2) in the ECDFS. The most common number of sources found is one (40%), followed by zero (33%). The highest number of sources found is six, and 95% of the regions contain four sources or fewer. This means that the surface density we measure in the field of MRC1138–262 is unusually high and we cannot find a similarly dense field in the entire ECDFS (almost 900 square arcmin).

To summarize, a comparison of the number counts suggests that we have detected a significant excess of SMGs in the field of MRC1138–262. However, is this overdensity connected to the protocluster structure at $z \approx 2.2$? In the following we discuss the evidence that the discovered overdensity is indeed associated with the protocluster at $z \approx 2.2$. Including the radio galaxy, five of the 16 SMGs (DKB01, DKB03, DKB07, DKB12, DKB16) are spectroscopically confirmed members of the protocluster at $z \approx 2.2$. A further two SMGs (DKB02, DKB15) have photometric redshifts that suggest they could be protocluster members. Our data excludes possible protocluster membership for three sources (DKB06, DKB13, DKB14). For the remaining six sources (DKB04, DKB05, DKB08, DKB09, DKB10, DKB11),

we cannot make a judgement on protocluster membership based on the data in hand. At least seven and up to 13 SMGs belong to the protocluster at $z \approx 2.2$.

All six spectroscopically confirmed SMG members of the protocluster structure at $z \approx 2.2$ — five LABOCA sources plus the CO-bright HAE associated with SCUBA emission — are located within a circle of $240''$ diameter, corresponding to 2.0 Mpc. In addition, both of the possible members, DKB02 and DKB15 also lie within this area. Calculating the surface density in this area as before (three sources fulfilling the flux density limit of 7.0 mJy and detection level of 3.7σ (following Weiß et al., 2009), two of them are spectroscopically confirmed protocluster members), we derive a surface density of $0.239 \text{ arcmin}^{-2}$, a factor of 4.3 higher than expected in a blank field at this wavelength.

Assuming a sphere of 2 Mpc, we calculate a SFRD of $\sim 1500 \text{ M}_\odot \text{ yr}^{-1} \text{ Mpc}^{-3}$ which is four orders of magnitude greater than the global SFRD at this redshift (Hopkins & Beacom, 2006). The SFRD of our protocluster is similar to results obtained by Clements et al. (2014) for two clumps of HerMES sources at $z = 2$.

The detection of an overdensity of SMGs at $z \approx 2.2$ is consistent with the overdensity of *Herschel* SPIRE $500 \mu\text{m}$ sources found by Rigby et al. (2014). We note that none of our LABOCA sources are located in the region where Valtchanov et al. (2013) reported an excess of SPIRE $250 \mu\text{m}$ sources at 5σ at a similar redshift $7'$ south of the protocluster structure. Several groups have previously found excesses of SMGs near HzRGs and QSOs (e.g., Ivison et al., 2000; Stevens et al., 2003; De Breuck et al., 2004; Greve et al., 2007; Priddey et al., 2008; Stevens et al., 2010; Carrera et al., 2011). In comparison to our work, none of them have direct probes that a significant fraction of their sources also lie at the redshift of the targeted HzRG or QSO.

Blain et al. (2004) report an association of five sources in the HDF-North. All five SMGs have spectroscopically measured redshifts of $z = 1.99$ (see also Chapman et al., 2009). This is the largest blank field SMG association known so far. It is spatially distributed on a larger region on the sky than the MRC1138–262 group, spanning a region of $7'$ (~ 3.5 Mpc) on a side. Chapman et al. (2009) report an apparently less significant overdensity of UV-selected galaxies at the same redshift and region of the sky. Another association of three SMGs lies in the same field but at $z \approx 4.0$ (Daddi et al., 2009a,b). To summarize, the protocluster at $z \approx 2.2$ is securely traced by galaxy populations probing different mass ranges, star formation and degree of obscuration including LAEs, HAEs, EROs and SMGs in the protocluster. Rigby et al. (2014) observe several known protocluster structures with SPIRE but do not recover SMG overdensities for many of them. On average they detect more SPIRE sources than compared to a blank field, and they detect an overdensity of SPIRE $500 \mu\text{m}$ sources in the MRC1138–262 field. Focusing on HyLIRGs selected from *Herschel* wide field imaging, Ivison et al. (2013) discovered a cluster of star-bursting proto-ellipticals at $z = 2.41$. Smail et al. (2014) related 31 FIR-/submm-selected sources to the $z = 1.62$ cluster Cl0218.3–0510. Contrarily, Beelen et al. (2008) report APEX LABOCA observations of the J2142–4423 Ly α protocluster at $z = 2.38$ and do not find an excess of SMGs in this field. Similarly, *Herschel* SPIRE observations by Wylezalek et al. (2013) do not confirm the previously reported SMG overdensity in the field of 4C+41.17 (Ivison et al., 2000). Overall, there is significant evidence both from our work and from the literature that the detection of large scale structures in the early universe by far-infrared/submm observation are feasible but still not common.

Koyama et al. (2013a) find a clustering of HAEs around the radio galaxy MRC1138–262 and report a large filament from north-east to south-west ($\gtrsim 10$ Mpc); a part of this filament was seen in the data of Kurk et al. (2004b). The SMGs belonging to the protocluster at $z \approx 2.2$ are distributed within the north-east filament (Kurk et al., 2004b; Koyama et al., 2013a) and the possible extension to the south-east (Koyama et al., 2013a) but not within the filament towards the south-west. However, due to the low number statistic, we cannot make a firm statement if the cosmic web could be traced by our SMGs. Our SMG overdensity is not centered on the radio galaxy, which lies at the western edge of the SMG concentration (see Fig. 9). A radial source density analysis strengthens this finding. This is in contrast to the four passive quiescent galaxies which cluster within 0.5 Mpc of the radio galaxy (Tanaka et al., 2013). The following hypothesis could explain these findings: both populations are massive but those in the centre have lost their gas; those that are still infalling have gas and are possibly being disturbed which makes them more active (see e.g. Verdugo et al., 2012, for details on this kind of scenario at low redshift). The HAE and SMG centres seem to be inconsistent, see Fig. 9. This finding is similar to that of Koyama et al. (2013b) for a cluster at $z = 0.4$ where a higher SFR is measured by the IR in the cluster center whereas the SFR derived from H α is similar to that of the field. Their conclusion is that the dust extinction in galaxies in high density regions is higher than those in the field, at the same redshift.

7. Conclusions

We have mapped the field of MRC1138–262 (~ 140 arcmin²) with APEX LABOCA at 870 μ m. This field has an exquisite multiwavelength dataset, close in quality to the ECDFS, including optical-NIR (VLT and Subaru), *Herschel* PACS+SPIRE, *Spitzer* IRAC, MIPS 24 μ m, and deep HST and VLA 1.4 GHz imaging, as well as VLT FORS2, ISAAC and SINFONI spectroscopy of protocluster members.

- In total, we detected 16 SMGs — 12 solid 3.5σ and 4 cross-identified tentative detections — with flux densities in the range 3–11 mJy. This is approximately a factor up to four more than expected from blank field surveys such as LESS (Weiß et al., 2009), — based on six sources with $S_{870\mu\text{m}} > 7$ mJy and $> 3.7\sigma$ significance level. This excess is consistent with the excess of SPIRE 500 μ m sources found by Rigby et al. (2014) at larger scales.
- Based on VLA 1.4 GHz, *Herschel*, *Spitzer* MIPS and Subaru rest-frame H α imaging at $z \sim 2.2$, we have identified the counterparts of the LABOCA sources and derived reliable far-infrared photometric redshifts. 55% of the SMGs with $z \approx 2.2$ H α imaging coverage are associated with HAEs. Near-infrared spectroscopic observations with VLT ISAAC and SINFONI have confirmed redshift to be $z = 2.16$ for four of these SMG counterparts. Including the radio galaxy, five out of 16 SMGs are secure protocluster members at $z \approx 2.2$. Another two SMGs have photometric redshifts suggesting that they are possible protocluster members. Our data excludes the protocluster membership for three SMGs. For the remaining six SMGs we do not have enough data to make a robust judgement on their protocluster membership.
- We associate the spectroscopically confirmed HAE229 (Kurk et al., 2004b) at $z = 2.149$, recently detected in CO(1-0) Emonts et al. (2013), with a SCUBA source (Stevens et al., 2003). This source is detected in *Herschel* bands and the far-IR photo- z is consistent with its spectroscopic redshift. Thus, we

conclude that this CO-bright HAE is an SMG related to the protocluster at $z \approx 2.2$, increasing the number of spectroscopically confirmed SMGs as protocluster members to six.

- All six spectroscopically confirmed members of the protocluster structure at $z \approx 2.2$ are located within a circle of $\sim 240''$ diameter, corresponding to 2.0 Mpc at this redshift. Both of the possible members, DKB02 and DKB15, also lie within this area. The excess of SMGs in this region is at least four times higher than expected from blank fields. For comparison, the surface density of LABOCA sources is significantly higher than the well known structure of six SMGs at $z = 1.99$ in GOODS-N distributed over 7×7 Mpc² (Blain et al., 2004; Chapman et al., 2009). The SMG overdensity is not centered on the radio galaxy, which lies at the edge of the dusty starburst concentration. The spatial distribution of the SMG overdensity seems to be similar to the north-east and south-east filament-like structure traced by HAEs (Kurk et al., 2004b; Koyama et al., 2013a). The SFR_{FIR} of the LABOCA sources related to the protocluster ranges between 200 to 1800 $\text{M}_{\odot} \text{yr}^{-1}$ and sums up to a star formation rate density $\text{SFRD} \sim 1500 \text{M}_{\odot} \text{yr}^{-1} \text{Mpc}^{-3}$, four magnitudes higher than the global SFRD at this redshift in the field.

Our results demonstrate that submillimeter observations can reveal clusters of massive, dusty starbursts. We show that at submm wavelengths systematic and detailed investigations of distant clusters are possible. However, we emphasize that only sensitive subarcsecond resolution observations with ALMA will allow a complete characterization of the 16 SMGs discovered by LABOCA.

Acknowledgements. Based on observations made with ESO Telescopes at Chajnantor and Paranal under programme 084.A-1016(A), 083.F-0022, 088.A-0754(A) and 090.B-712(A). This work is based on observations with the APEX telescope. APEX is a collaboration between the Max-Planck-Institut für Radioastronomie, the European Southern Observatory, and the Onsala Observatory. We are very grateful to Ian Smail who encouraged us to carry out this project and gave helpful advice during the project. We are much obliged to instructive help by Bjorn Emonts regarding the CO(1-0) observations of HAE229. We would like to thank the APEX staff for their support during the observations and Chris Carilli for his help during the VLA data reduction. The National Radio Astronomy Observatory is a facility of the National Science Foundation operated under cooperative agreement by Associated Universities, Inc. We also acknowledge the contribution by the anonymous referee in clarifying a number of important points and thus improving this manuscript. We are grateful to Elaine Grubmann for proofreading. This publication is supported by the Austrian Science Fund (FWF). NS is supported by an ARC Future Fellowship. *Herschel* is an ESA space observatory with science instruments provided by European-led Principal Investigator consortia and with important participation from NASA. PACS has been developed by a consortium of institutes led by MPE (Germany) and including UVIE (Austria); KU Leuven, CSL, IMEC (Belgium); CEA, LAM (France); MPIA (Germany); INAF-IFSI/OAA/OAP/OAT, LENS, SISSA (Italy); IAC (Spain). This development has been supported by the funding agencies BMVIT (Austria), ESA-PRODEX (Belgium), CEA/CNES (France), DLR (Germany), ASI/INAF (Italy), and CICYT/MCYT (Spain). SPIRE has been developed by a consortium of institutes led by Cardiff University (UK) and including Univ. Lethbridge (Canada); NAOC (China); CEA, LAM (France); IFSI, Univ. Padua (Italy); IAC (Spain); Stockholm Observatory (Sweden); Imperial College London, RAL, UCL-MSSL, UKATC, Univ. Sussex (UK); and Caltech, JPL, NHSC, Univ. Colorado (USA). This development has been supported by national funding agencies: CSA (Canada); NAOC (China); CEA, CNES, CNRS (France); ASI (Italy); MCINN (Spain); SNSB (Sweden); STFC (UK); and NASA (USA).

References

- Amblard, A., Cooray, A., Serra, P., et al. 2010, *A&A*, 518, L9
- Barger, A. J., Wang, W.-H., Cowie, L. L., et al. 2012, *ApJ*, 761, 89
- Beelen, A., Omont, A., Bavouzet, N., et al. 2008, *A&A*, 485, 645
- Best, P. N., Lehnert, M. D., Miley, G. K., Röttgering, H. J. A. 2003, *MNRAS*, 343, 1
- Biggs, A. D., Ivison, R. J., Ibar, E., et al. 2011, *MNRAS*, 413, 2314

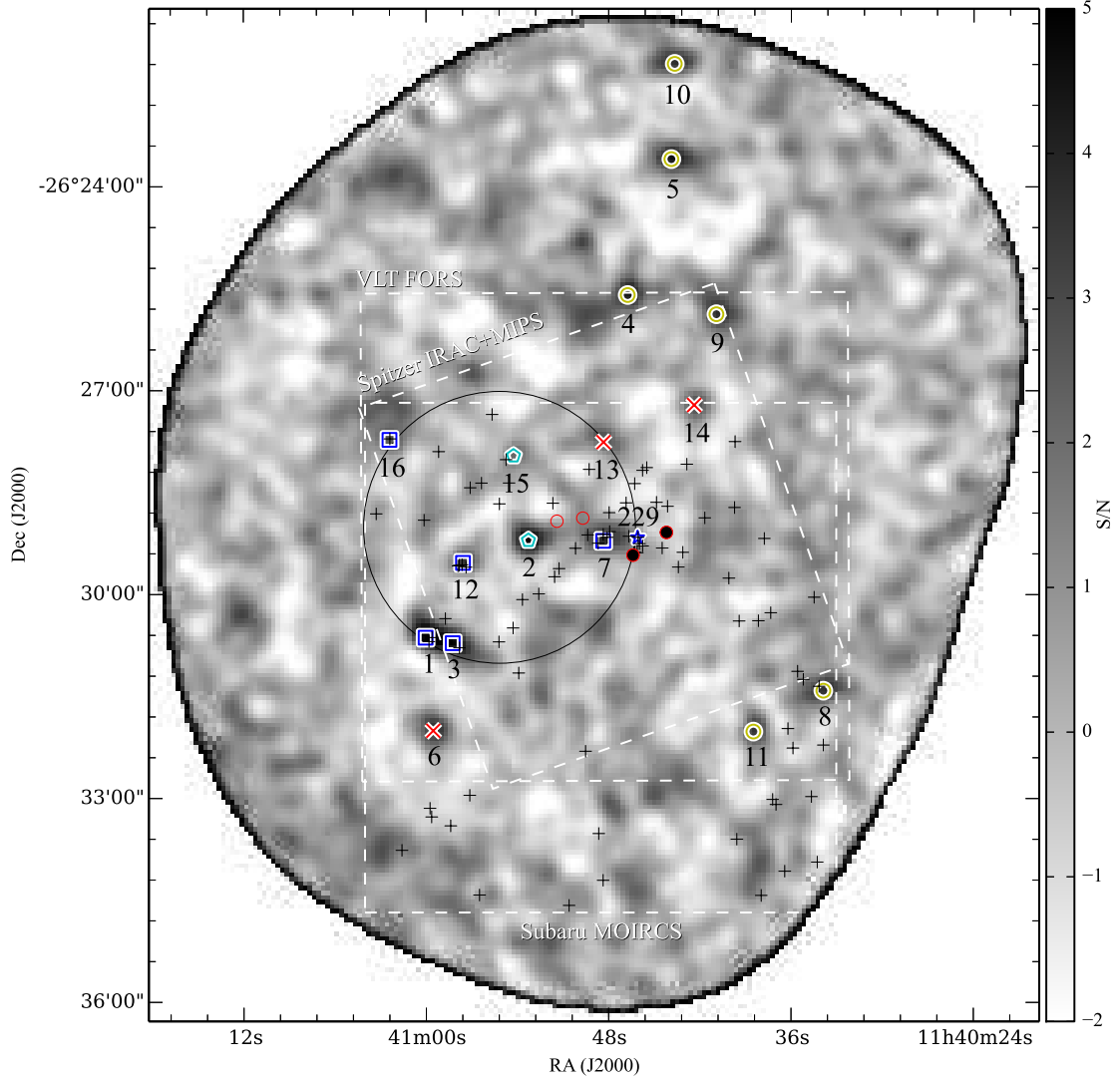


Fig. 9. The location of 16 SMGs extracted from our LABOCA map of the field of MRC1138 on top of the LABOCA signal-to-noise map. Blue squares represent spectroscopically confirmed membership to the protocluster structure at $z \approx 2.2$. The blue star is the SCUBA source at $z = 2.149$, also detected in CO(1-0) by Emonts et al. (2013). Cyan pentagons show possible protocluster members. In the case of yellow circles, no reliable judgment on the cluster membership can be made. Red crosses are sources that can be securely excluded from the protocluster. The large circle has a diameter of $\sim 240''$ (corresponding to a physical size 2 Mpc) and shows the region where all eight SMGs at $z = 2.2$ are located. The SMG overdensity is at least a factor four higher than compared to blank fields (Weiß et al., 2009) and not centered on the radio galaxy MRC1138 (DKB07). The spatial distribution of the SMG overdensity seems to be similar to the north-east and south-east filament-like structure traced by HAEs (plus symbols Kurk et al., 2004b; Koyama et al., 2013a) and in contrast to the location of passive quiescent galaxies clustered within 0.5 Mpc around the radio galaxy (red circles, filled if spectroscopically confirmed, see Tanaka et al., 2013). In addition, we show the fields of view of our *Spitzer* IRAC/MIPS, VLT FORS and Subaru MOIRCS datasets. North is at the top and east is to the left.

Blain, A. W., Smail, I., Ivison, R. J., Kneib, J.-P., & Frayer, D. T. 2002, *Phys. Rep.*, 369, 111
 Blain, A. W., Chapman, S. C., Smail, I., & Ivison, R. 2004, *ApJ*, 611, 725
 Bolzonella, M., Miralles, J.-M., & Pelló, R. 2000, *A&A*, 363, 476
 Carrera, F. J., Page, M. J., Stevens, J. A., et al. 2011, *MNRAS*, 413, 2791
 Casey, C. M. 2012, *MNRAS*, 425, 3094
 Chabrier, G. 2003, *PASP*, 115, 763
 Chapman, S. C., Blain, A. W., Smail, I., & Ivison, R. J. 2005, *ApJ*, 622, 772
 Chapman, S. C., Blain, A., Ibata, R., et al. 2009a, *ApJ*, 691, 560
 Clements, D., et al. 2014, *MNRAS*, 439, 1139
 Croft, S., Kurk, J., van Breugel, W., et al. 2005, *AJ*, 130, 867
 Daddi, E., Dickinson, M., Morrison, G., et al. 2007, *ApJ*, 670, 156
 Daddi, E., Dannerbauer, H., Stern, D., et al. 2009a, *ApJ*, 694, 1517
 Daddi, E., Dannerbauer, H., Krips, M., et al. 2009b, *ApJ*, 695, L176
 Dannerbauer, H., Lehnert, M. D., Lutz, D., et al. 2002, *ApJ*, 573, 473

Dannerbauer, H., Lehnert, M. D., Lutz, D., et al. 2004, *ApJ*, 606, 664
 Dannerbauer, H., Daddi, E., Morrison, G. E., et al. 2010, *ApJ*, 720, L144
 De Breuck, C., Bertoldi, F., Carilli, C., et al. 2004, *A&A*, 424, 1
 Dole, H., Lagache, G., Puget, J.-L., et al. 2006, *A&A*, 451, 417
 Downes, A. J. B., Peacock, J. A., Savage, A., & Carrie, D. R. 1986, *MNRAS*, 218, 31
 Emonts, B. H. C., Feain, I., Röttgering, H. J. A., et al. 2013, *MNRAS*, 430, 3465
 Fomalont, E. B., Kellermann, K. I., Cowie, L. L., et al. 2006, *ApJS*, 167, 103
 Fu, H., Jullo, E., Cooray, A., et al. 2012, *ApJ*, 753, 134
 Galametz, A., Vernet, J., De Breuck, C., et al. 2010, *A&A*, 522, A58
 Galametz, A., Stern, D., De Breuck, C., et al. 2012, *ApJ*, 749, 169
 Genzel, R., Baker, A. J., Tacconi, L. J., et al. 2003, *ApJ*, 584, 633
 Greve, T. R., Bertoldi, F., Smail, I., et al. 2005, *MNRAS*, 359, 1165
 Greve, T. R., Stern, D., Ivison, R. J., et al. 2007, *MNRAS*, 382, 48
 Griffin, M. J., Abergel, A., Abreu, A., et al. 2010, *A&A*, 518, L3

- Hainline, L. J., Blain, A. W., Smail, I., et al. 2009, *ApJ*, 699, 1610
- Hatch, N. A., De Breuck, C., Galametz, A., et al. 2011a, *MNRAS*, 410, 1537
- Hatch, N. A., Kurk, J. D., Pentericci, L., et al. 2011b, *MNRAS*, 415, 2993
- Herranz, D., González-Nuevo, J., Clements, D. L., et al. 2013, *A&A*, 549, A31
- Hickox, R. C., Wardlow, J. L., Smail, I., et al. 2012, *MNRAS*, 421, 284
- Hodge, J. A., Karim, A., Smail, I., et al. 2013, *ApJ*, 768, 91
- Hopkins, A. M., & Beacom, J. F. 2006, *ApJ*, 651, 142
- Intema, H. T., Venemans, B. P., Kurk, J. D., et al. 2006, *A&A*, 456, 433
- Ivison, R. J., Dunlop, J. S., Smail, I., et al. 2000, *ApJ*, 542, 27
- Ivison, R. J., Greve, T. R., Smail, I., et al. 2002, *MNRAS*, 337, 1
- Ivison, R. J., Morrison, G. E., Biggs, A. D., et al. 2008, *MNRAS*, 390, 1117
- Ivison, R. J., Smail, I., Amblard, A., et al. 2012, *MNRAS*, 425, 1320
- Ivison, R. J., Swinbank, A. M., Smail, I., et al. 2013, *ApJ*, 772, 137
- Jones, D. H., Read, M. A., Saunders, W., et al. 2009, *MNRAS*, 399, 683
- Karim, A., Swinbank, M., Hodge, J., et al. 2013, *MNRAS*, 432, 2
- Kennicutt, R. C., Jr. 1998, *ApJ*, 498, 541
- Koyama, Y., Kodama, T., Shimasaku, K., et al. 2010, *MNRAS*, 403, 1611
- Koyama, Y., Kodama, T., Tadaki, K.-i., et al. 2013a, *MNRAS*, 428, 1551
- Koyama, Y., Smail, I., Kurk, J., et al. 2013b, *MNRAS*, 434, 423
- Kovács, A. 2008, *Proc. SPIE*, 7020, 45
- Kuiper, E., Hatch, N. A., Miley, G. K., et al. 2011, *MNRAS*, 415, 2245
- Kurk, J. D., Röttgering, H. J. A., Pentericci, L., et al. 2000, *A&A*, 358, L1
- Kurk, J. D., Pentericci, L., Röttgering, H. J. A., & Miley, G. K. 2004a, *A&A*, 428, 793
- Kurk, J. D., Pentericci, L., Overzier, R. A., Röttgering, H. J. A., & Miley, G. K. 2004b, *A&A*, 428, 817
- Lagache, G., Puget, J.-L., & Dole, H. 2005, *ARA&A*, 43, 727
- Le Fevre, O., Deltorn, J. M., Crampton, D., & Dickinson, M. 1996, *ApJ*, 471, L11
- Lutz, D., Dunlop, J. S., Almaini, O., et al. 2001, *A&A*, 378, 70
- Lutz, D., Poglitsch, A., Altieri, B., et al. 2011, *A&A*, 532, A90
- Matsuda, Y., Yamada, T., Hayashino, T., et al. 2005, *ApJ*, 634, L125
- Matsuda, Y., Smail, I., Geach, J. E., et al. 2011, *MNRAS*, 416, 2041
- Mayo, J. H., Vernet, J., De Breuck, C., et al. 2012, *A&A*, 539, A33
- Miley, G. K., Overzier, R. A., Zirm, A. W., et al. 2006, *ApJ*, 650, L29
- Miley, G., & De Breuck, C. 2008, *A&A Rev.*, 15, 67
- Morrison, G. E., Owen, F. N., Dickinson, M., Ivison, R. J., & Ibar, E. 2010, *ApJS*, 188, 178
- Moshir, M., & et al. 1990, *IRAS Faint Source Catalogue*, version 2.0 (1990), 0
- Napier, P., Thompson, A., & Ekers, R. 1983, *Proc. IEEE*, 71, 1295
- Noble, A. G., Geach, J. E., van Engelen, A. J., et al. 2013, *MNRAS*, 436, L40
- Ouchi, M., Shimasaku, K., Okamura, S., et al. 2004, *ApJ*, 611, 685
- Oteo, I., Bongiovanni, A., Pérez García, A. M., et al. 2012, *A&A*, 541, A65
- Overzier, R. A., Miley, G. K., Bouwens, R. J., et al. 2006, *ApJ*, 637, 58
- Pearson, E. A., Eales, S., Dunne, L., et al. 2013, *MNRAS*, 435, 2753
- Pentericci, L., Kurk, J. D., Röttgering, H. J. A., et al. 2000, *A&A*, 361, L25
- Pentericci, L., Kurk, J. D., Carilli, C. L., et al. 2002, *A&A*, 396, 109
- Perrault, M., 1987, *Structure et evolution des nuages moleculaire*, PhD-Thesis, Univ. Paris
- Pilbratt, G. L., Riedinger, J. R., Passvogel, T., et al. 2010, *A&A*, 518, L1
- Poglitsch, A., Waelkens, C., Geis, N., et al. 2010, *A&A*, 518, L2
- Polletta, M., Tajer, M., Maraschi, L., et al. 2007, *ApJ*, 663, 81
- Pope, A., Scott, D., Dickinson, M., et al. 2006, *MNRAS*, 370, 1185
- Priddey, R. S., Ivison, R. J., & Isaak, K. G. 2008, *MNRAS*, 383, 289
- Rigby, E. E., Hatch, N. A., Röttgering, H. J. A., et al. 2014, *MNRAS*, 437, 1882
- Roseboom, I. G., Ivison, R. J., Greve, T. R., et al. 2012, *MNRAS*, 419, 2758
- Santini, P., Fontana, A., Grazian, A., et al. 2009, *A&A*, 504, 751
- Seymour, N., Altieri, B., De Breuck, C., et al. 2012, *ApJ*, 755, 146
- Shapley, A. E., Steidel, C. C., Pettini, M., & Adelberger, K. L. 2003, *ApJ*, 588, 65
- Shimakawa, R., Kodama, T., Tadaki, K.-i., et al. 2014, *MNRAS*, 441, L1
- Siringo, G., Kreysa, E., Kovács, A., et al. 2009, *A&A*, 497, 945
- Skibba, R. A., Engelbracht, C. W., Dale, D., et al. 2011, *ApJ*, 738, 89
- Smail, I., Ivison, R. J., & Blain, A. W. 1997, *ApJ*, 490, L5
- Smail, I., Swinbank, A. M., Ivison, R. J., & Ibar, E. 2011, *MNRAS*, 414, L95
- Smail, I., Geach, J. E., Swinbank, A. M., et al. 2014, *ApJ*, 782, 19
- Spergel, D. N., Verde, L., Peiris, H. V., et al. 2003, *ApJS*, 148, 175
- Spergel, D. N., Bean, R., Doré, O., et al. 2007, *ApJS*, 170, 377
- Steidel, C. C., Adelberger, K. L., Dickinson, M., et al. 1998, *ApJ*, 492, 428
- Stern, D., Jimenez, R., Verde, L., Kamionkowski, M., & Stanford, S. A. 2010, *J. Cosmology Astropart. Phys.*, 2, 8
- Stevens, J. A., Ivison, R. J., Dunlop, J. S., et al. 2003, *Nature*, 425, 264
- Stevens, J. A., Jarvis, M. J., Coppin, K. E. K., et al. 2010, *MNRAS*, 405, 2623
- Swinbank, A. M., Smail, I., Chapman, S. C., et al. 2004, *ApJ*, 617, 64
- Swinbank, A. M., Simpson, J. M., Smail, I., et al. 2014, *MNRAS*, 438, 1267
- Tanaka, M., De Breuck, C., Venemans, B., & Kurk, J. 2010, *A&A*, 518, A18
- Tanaka, M., et al. 2013, *ApJ*, 772, 113
- Taylor, G., Carilli, C., & Perley, R. 1999, *ASP Conf. Ser.* 180: *Synthesis Imaging in Radio Astronomy II*
- Valtchanov, I., et al. 2013, *MNRAS*, 436, 2505
- Venemans, B. P., Kurk, J. D., Miley, G. K., et al. 2002, *ApJ*, 569, L11
- Venemans, B. P., Röttgering, H. J. A., Overzier, R. A., et al. 2004, *A&A*, 424, L17
- Venemans, B. P., Röttgering, H. J. A., Miley, G. K., et al. 2005, *A&A*, 431, 793
- Venemans, B. P., Röttgering, H. J. A., Miley, G. K., et al. 2007, *A&A*, 461, 823
- Verdugo, M., Lerchster, M., Böhringer, H., et al. 2012, *MNRAS*, 421, 1949
- Walter, F., Decarli, R., Carilli, C., et al. 2012, *Nature*, 486, 233
- Wardlow, J. L., Smail, I., Coppin, K. E. K., et al. 2011, *MNRAS*, 415, 1479
- Webb, T. M., Eales, S. A., Lilly, S. J., et al. 2003a, *ApJ*, 587, 41
- Webb, T. M. A., Lilly, S. J., Clements, D. L., et al. 2003b, *ApJ*, 597, 680
- Weiß, A., Kovács, A., Coppin, K., et al. 2009, *ApJ*, 707, 1201
- Wylezalek, D., Vernet, J., De Breuck, C., et al. 2013, *MNRAS*, 428, 3206
- Younger, J. D., Fazio, G. G., Huang, J.-S., et al. 2007, *ApJ*, 671, 1531